3 In Vivo Two-Photon Laser Scanning Microscopy with Concurrent Plasma-Mediated Ablation

Principles and Hardware Realization

Philbert S. Tsai and David Kleinfeld

CONTENTS

3.1 INTRODUCTION

Many biological processes of current interest occur below the surface layers of accessible tissue. It is often the case that the surface layers cannot easily be removed without adversely affecting the physiology and function of the deeper layers. A variety of imaging techniques have been developed to perform sectioning deep to the surface using optical, electrical, and magnetic contrast agents and recording methods. Two-photon laser scanning microscopy (TPLSM) with ultrashort (i.e., order 100-fs) pulsed laser light provides optically sectioned images from depths of 500 microns or more below the surface in highly scattering brain tissue.[1–5] This method is unique in that it can provide images with submicrometer lateral resolution and micrometer axial resolution on the millisecond time-scale,[6] as is required for the study of many dynamic biological processes.[1,7–11]

A strength of TPLSM is the ease with which this technique may be combined with electrical measurements of physiological parameters and with other optical techniques. These include one-photon uncaging with gated continuous laser light, two-photon uncaging with ultrashort pulsed laser light and, of particular interest in this work, plasma-mediated ablation through the nonlinear absorption of amplified ultrashort laser pulses.

A nonlinear interaction that is of particular relevance for the ablation of submicrometer volumes of neuronal[12] and vascular[13] tissue deep in the brain is plasma-mediated ablation.[14–16] Here, the optical field of the ultrashort pulse leads to a high rate of tunneling by electrons to form an electron plasma.[17] The density of this plasma rapidly builds up by virtue of field-driven collisions between free electrons and molecules, while the thickness of the plasma approaches a value that is much less than the depth of the focal volume. The absorption of laser light by this thin layer leads to highly localized ablation and the explosive removal of material. One critical feature of plasma-mediated ablation is that light outside of the focal volume has little detrimental effect on the specimens; this limits the thermal build-up and ensuing collateral damage in the targeted tissue.

This chapter provides an overview of the technical considerations relevant to the design and assembly of a system for TPLSM that is particularly suitable for in vivo imaging and histology, either alone or in combination with plasma-mediated ablation. It extends an earlier technical presentation[18] and complements other designs of upright systems.[19–21] The conversion of commercially available confocal microscopes for use in TPLSM, rather than the de novo construction of a system, have been described.[22–26] Commercial systems for TPLSM are available from Prairie (Ultima; www.prairie-technologies.com) and Leica (TPS MP; www.leica.com), and it is likely that the commercial market will continue to mature. Commercial systems that incorporate amplified ultrashort laser pulses do not exist at this time, although it should be simple to adapt current systems to support two beams.

3.2 OVERVIEW

3.2.1 SINGLE PHOTON ABSORPTION FOR IMAGING THROUGH WEAKLY SCATTERING PREPARATIONS

In traditional fluorescence microscopy, including confocal microscopy, fluorescent molecules that are either intrinsic to the tissue or artificially introduced are excited by a wavelength of light that falls within the linear absorption spectrum of the molecule. A single photon is absorbed by the molecule and promotes it to an excited electronic state. Upon thermal equilibration and relaxation back to its ground state, the molecule will emit a photon that is shifted toward longer wavelengths with respect to the excitation light.

The probability of exciting fluorescence by the absorption of a single photon is linearly proportional to the spatial density of photons (i.e., the light intensity). The total fluorescence is, therefore, constant from any given axial plane (i.e., a plane taken normal to the propagation direction), regardless of the focusing of the incident beam. As one moves toward the focus of a beam, its intensity in a given axial plane increases as the power becomes distributed over a smaller cross-sectional area. At the same time, fewer fluorescent molecules in that plane are exposed to the illumination, so that the lateral extent of the excitation is reduced.

3.2.1.1 Direct Imaging

Biological preparations that do not appreciably scatter or absorb the incident light, such as in vitro slice or cell culture, can be observed by a variety of direct imaging techniques,[27] typically with the use of a charge coupled device array detector. In whole-field fluorescent microscopy, the entire region of interest in the preparation is concurrently illuminated, and all of the collected fluorescent light is recorded. This method has the advantage of a high rate of data collection (e.g., hundreds of frames per second with current array detectors), but suffers from the lack of optical sectioning. The fluorescence generated from planes outside the focal plane contributes in a nonuniform manner to the background level. The result is a lack of axial resolution and a signal-to-noise ratio that is lower than for an image in which fluorescence from outside the focal plane is eliminated.

Axial resolution on the order of the diffraction limit may, in principle, be achieved with direct imaging methods in which light from regions outside the focal plane is systematically eliminated (Table 3.1). One method is to acquire data at multiple depths, by shifting the focus above and below the object plane, and then use the images from out-of-focus planes, in conjunction with a deconvolution procedure, to model and subtract the out-of focus light.[28–31] This method and its extensions have the advantage of experimental simplicity in that only a motorized focus control need be added to a standard microscope. On the other hand, diffraction by the open aperture of the objective leads to a set of dark rings in the transfer function of the objective so that this method is insensitive to the spatial frequencies of these rings. This is the so-called "missing cone" problem in which the cone represents spatial frequencies in radial and axial momentum space (i.e., k_r and k_z). An alternate procedure is to project a line grating into the object plane so that the projected image has spacing on the order of the lateral

TABLE 3.1

Nominal Properties of Techniques for Functional Imaging with Fluorescent Indicators

Mode	Technique	Axial Resolution	Lateral Resolution	Frame Period (100 by 100 pixels)	Depth Penetration
Direct image formation (CCD acquisition)	Full field	$\gg\lambda$	*λ	~100 Hz	~$\Lambda_{scattering}$
	Vibrating grating	~λ		<30 Hz	
	Deconvolution				
	Interferometric	$\ll\lambda$			$\ll\Lambda_{scattering}$
Point scanning (PMT acquisition)	Confocal	~λ		~10 Hz >100 Hz (resonant or AOM line scan)	~$\Lambda_{scattering}$
	Multiphoton excitation				$\gg\Lambda_{scattering}$

diffraction limit. When this grating is modulated in time, only the part of the signal that emanates from the object plane is concurrently modulated. Thus, information about the intensity distribution only in the object plane may be extracted.[32,33] A final set of methods are applicable only to physically thin objects and rely on an interferometric cavity to set up an optical field that varies in the axial direction.[34,35] This may be used to achieve axial resolution on length-scales of less than one wavelength.

3.2.1.2 Confocal Laser Scanning Microscopy

Laser scanning microscopy provides an improved means to achieve axial resolution compared with direct imaging techniques. An incoming laser beam is deflected by a pair of rotating mirrors, mounted at orthogonal angles, and is subsequently focused by a microscope objective onto the preparation. The angular deflection of the collimated laser beam causes the focused spot to move across the preparation in a specified raster pattern. The fluorescent light that is generated at the focal volume is collected by a detector as a function of time; this time series is transformed back into a position in the preparation along the trajectory of the spot. The drawback to laser scanning methods of microscopy is a reduced speed of acquisition compared with direct imaging techniques. The maximum acquisition rate is limited by the speed at which the scan mirrors can raster across the region of interest.

In confocal microscopy, axial resolution is obtained by preferentially collecting fluorescent light that is generated near the focal plane, while rejecting light that is generated outside the focal plane. Specifically, the fluorescent light is refocused along the same beam path as the excitation light. After passing back through the scan mirrors—a process referred to as "descanning"—the light is spatially filtered by a small aperture, or pinhole, whose radius is chosen so that its image in the preparation matches or exceeds the diffraction-limited radius of the illuminated region.

The pinhole preferentially passes fluorescent light generated near the focal plane. Although confocal microscopy works well for optically thin preparations, it is inefficient for preparations in which substantial scattering occurs. As the fluorescent light becomes more heavily scattered, a greater portion of the photons from the focal plane are deflected from their original trajectories and are thus blocked by the pinhole, remaining undetected. Conversely, an increasing portion of the light from outside the focal plane will be deflected to pass through the pinhole. The result is a drop in the signal-to-noise ratio.

3.2.2 Two-Photon Laser Scanning Microscopy for Strongly Scattering Preparations

Two-photon laser scanning microscopy utilizes laser light at approximately twice the wavelength of that used in traditional, one-photon microscopy. These photons carry half of the energy required to promote a molecule to its excited state, and thus the excitation process requires the simultaneous absorption of two photons from the excitation beam. The probability of two-photon absorption thus scales with the square of the incident laser intensity. This nonlinear absorption process provides an intrinsic mechanism for optical sectioning solely by the incident beam.

To gain a semi-quantitative understanding into the localized nature of two-photon excitation, consider the total fluorescence generated from a given cross-sectional plane, F_{total}. This is linearly proportional to the illuminated area, A, and a quadratic function of the incident intensity, I, defined as the incident laser power, P, divided by the area (i.e., $I = P/A$ [Figure 3.1]). The illuminated area in a given plane is proportional to the square of the axial distance of that plane from the focal plane (i.e., $A \propto z^2$) for z larger than the focal depth of the beam. Thus,

$$F_{total} \propto I^2 A \propto \left(\frac{P}{z} \right)^2 .$$

The amount of fluorescence that is generated from a given axial plane is seen to decrement as a quadratic function of the distance from the focal plane (Figure 3.2). The integrated fluorescence is thus finite, that is,

$$\int_{-\infty}^{+\infty} dz \; F_{total} \propto 2 \int_{z_{confocal}}^{+\infty} dz F_{total} \propto 2 \int_{z_{confocal}}^{+\infty} dz \left(\frac{P}{z} \right)^2 \rightarrow \text{Constant}$$

where $z_{confocal}$, defined later (Equation 3.2), is proportional to the focus depth. Only light within the focal region contributes significantly to the signal. Thus, with TPLSM all of the fluorescent light can be collected as signal, regardless of scattering. In contrast, the above integral diverges for single photon absorption.
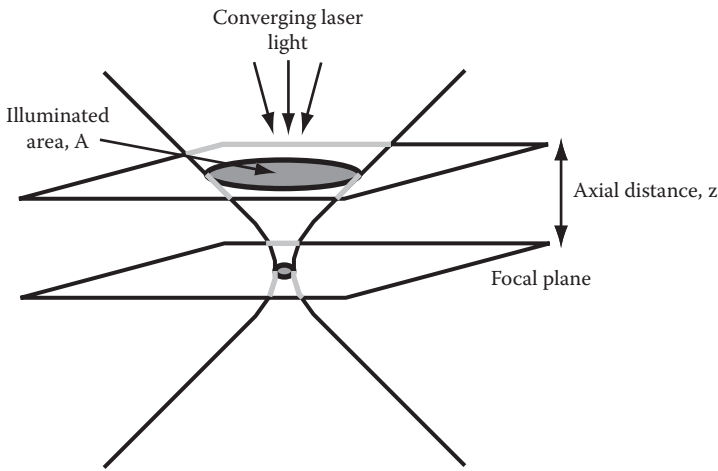
FIGURE 3.1   Cartoon of laser light near the focus of an objective. The shaded regions indicated the cross-sectional area in a given plane, normal to the direction of propagation, that is illuminated by the converging laser light. The illuminated cross-sectional area is seen to decrease as the distance to the focal plane decreases.
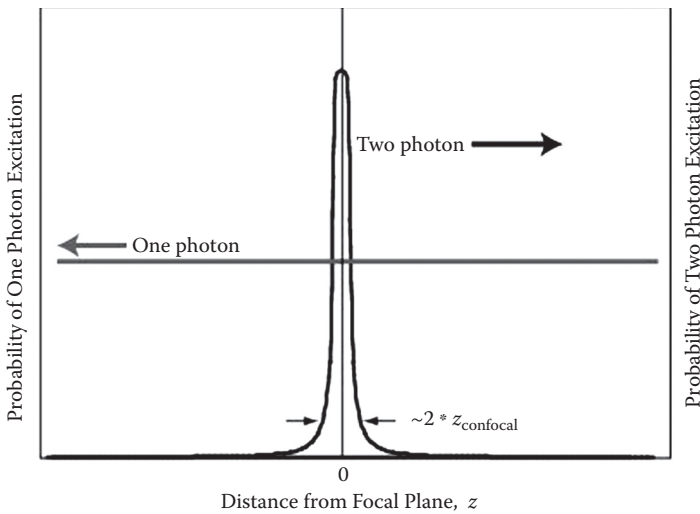
FIGURE 3.2   The integrated excitation of fluorphores within an axial plane as a function of the axial distance from the focus, denoted z. Single-photon excitation results in an excitation profile that is constant with axial distance (light line). Two-photon excitation results in an excitation profile that falls off quadratically with axial distance from the focal plane (dark line).

The probability of simultaneously absorbing two photons is small compared to the probability of single photon absorption at half the wavelength. Therefore, a pulsed laser source is necessary to provide the large incident peak intensities that are required to generate significant two-photon signals, while concurrently maintaining the average power at levels that avoid heating of the preparation. The use of ultrashort laser pulses allows for the greatest efficiency and depth penetration while reducing the potential for thermal damage to the preparation (but see Reference 36). In particular, the extent of thermal damage depends on the average power delivered by the incident beam, while the depth penetration is a function of the instantaneous peak power.

Two-photon laser scanning microscopy is uniquely suited for optically sectioning through thick preparations.[37] In brief:

1. The fluorescent signal is not descanned (i.e., the fluorescent light does not require spatial filtering with a pinhole, as for the case of confocal microscopy). This yields a higher collection efficiency for scattering preparations. It further permits a much simpler alignment of collection optics compared with confocal microscopy.
2. The use of near infrared light for two-photon excitation, as opposed to blue/ UV light for single-photon excitation, is preferable with biological preparations. Wavelengths in the near-infrared are less heavily scattered, as well as less likely to be absorbed by biological molecules. In particular, the flavins and other molecules involved in bioenergetics are far less excitable by near infrared light than by UV/blue light.
3. The two-photon spectra of fluorophores are generally broader than their one photon counterparts and are spectrally separated further from the fluorescence emission peak. Both of these characteristics simplify the technical task of separating the excitation and emission light and allow for the simultaneous excitation of multiple dyes with a single laser source.

3.3 BASICS

3.3.1 FOCAL VOLUMES

The fundamental optical length scale is the radius of the beam at the focus.[38] The relevant variables in deriving the imaging and ablation parameters are

$$\omega(z) \equiv \text{Radius of beam a distance z from focus}$$
$$\omega(0) \equiv \text{Radius of beam at the focus}$$
$$z_{confocal} \equiv \text{Confocal depth (i.e., axial distance for beam to double width)}$$
$$V_{excitation} \equiv \text{Optical excitation volume}$$
$$V_{ablation} \equiv \text{Plasma-mediated ablation volume}$$
$$\lambda_o \equiv \text{Center wavelength of laser}$$
$$\text{NA} \equiv \text{Numerical aperture of objective}$$
$$n \equiv \text{Optical index } (n = 1.33 \text{ for water})$$

$$P^{\text{incident}} \equiv \text{Incident laser power}$$
$$I^{\text{incident}}(r,z,t) \equiv \text{Incident laser intensity}$$
$$E \equiv \text{Energy of laser pulse}$$
$$\varepsilon \equiv \text{Normalized energy for plasma-mediated ablation}$$
$$F^{\text{incident}}(r,z) \equiv \text{Incident laser pulse}$$

The radius of the beam at the focus, $\omega(0)$, is

$$\omega(0) \;=\; \frac{1}{\pi}\,\frac{\lambda_o}{NA}\sqrt{1-\left(\frac{NA}{n}\right)^2} \;\xrightarrow[NA \ll n]{}\; \frac{1}{\pi}\frac{\lambda_o}{NA}\;. \qquad (3.1)$$

3.3.1.1 Excitation

The above expression for the radius of the beam (Equation 3.1) should be compared with the minimum lateral length-scale that can be resolved with planar illumination,[39] that is, $\lambda_o/(2 \cdot NA)$.[27] The confocal length is the distance for the beam to double in area, that is,

$$z_{\text{confocal}} \;=\; \frac{\pi\, n\, \omega^2(0)}{\lambda_o} = \frac{n}{\pi}\,\frac{\lambda_o}{(NA)^2}\left[1-\left(\frac{NA}{n}\right)^2\right]\xrightarrow[NA \ll n]{}\frac{n}{\pi}\,\frac{\lambda_o}{(NA)^2}\;; \quad (3.2)$$

this expression should be compared with the minimum axial length-scale that can be resolved with planar illumination,[39] that is, $(\lambda_o/n)\left[1-\sqrt{1-(NA/n)^2}\,\right]^{-1}\xrightarrow[NA \ll n]{}(2n\lambda_o)/(NA)^2$.[27] The effective excitation volume is

$$V_{\text{excitation}} = \pi\,\omega^2(0)\,2\,z_{\text{confocal}} = \frac{2n}{\pi^2}\,\frac{\lambda_o^3}{(NA)^4}\left[1-\left(\frac{NA}{n}\right)^2\right]^2\xrightarrow[NA \ll n]{}\frac{2n}{\pi^2}\,\frac{\lambda_o^3}{(NA)^4}\;. \quad (3.3)$$

For the practical case of a 40-times magnification water dipping lens with NA = 0.80 and a laser with 800 nm excitation light, the Gaussian-profile beam parameters are

$$\omega(0) = 0.25\ \mu\text{m},\ z_{\text{confocal}} \cong 0.35\ \mu\text{m},\ \text{and}\ V_{\text{excitation}} \cong 0.15\ \mu\text{m}^3.$$

3.3.1.2 Ablation

The volume of material removed by plasma-mediated optical ablation may be estimated in terms of the previously given length scales (Equations 3.1 to 3.3), the energy of the incident pulses, and a phenomenological value for the threshold fluence of ablation.[40] The intensity for a Gaussian beam that propagates along the z-axis is[38]

$$I^{\text{incident}}(r,z,t) = 2\left[\frac{P^{\text{incident}}(t)}{\pi\omega^2(z)}\right]e^{-2r^2/\omega^2(z)} \qquad (3.4)$$

The relevant parameterization for cutting is the fluence,

$$F^{\text{incident}}(r,z) \equiv \int_{-\infty}^{\infty} dt\; I^{\text{incident}}(r,z,t) = 2\left[\frac{E}{\pi\omega^2(z)}\right]e^{-2r^2/\omega^2(z)}, \qquad (3.5)$$

where the energy per pulse is

$$E = \int_{-\infty}^{\infty} dt \int_{0}^{\infty} r\,dr \int_{-\pi}^{\pi} d\theta\; I(r,0,t). \qquad (3.6)$$

The dependence of the fluence on the axial distance is simplified for the paraxial approximation, valid for NA << n, that is,

$$\omega(z) = \omega(0)\sqrt{1 + \left(\frac{NA}{n}\frac{z}{\omega(0)}\right)^2}. \qquad (3.7)$$

We denote the threshold value of the fluence at the focus as F_T. The extent of the ablated region along the z-axis is found from $F_T = 2E/[\pi\omega^2(z_T)]$, for which $z_T = \omega(0)\left(\frac{n}{NA}\right)\sqrt{\varepsilon - 1}$ where

$$\varepsilon = \frac{2E}{\pi\;\omega^2(0)\;F_T} \qquad (3.8)$$

is the normalized energy per pulse and ablation requires $\varepsilon > 1$. The ablation volume with the focal plane below the surface of the tissue is given by

$$V_{ablation} = \int_{-z_T}^{+z_T} dz\; \pi r^2(z) \;=\; \pi\; \omega^3(0)\left(\frac{n}{NA}\right)\int_{0}^{x_T} dx\; (1+x^2)\; \ln\left(\frac{1+x_T^2}{1+x^2}\right), \qquad (3.9)$$

where $r(z)$ is the radius for which the fluence of the beam equals F_T, and we inverted the expression for $F(r,z)$ and normalized the integration variable, with $x_T = \sqrt{\varepsilon - 1}$. Although the integral can be done exactly, extrapolation beyond the threshold fluence is appropriate only for small values of x_T or, equivalently, for ε close to 1. We thus find our essential result,

$$V_{ablation}^{\substack{\text{minimum}}} \xrightarrow[\varepsilon\approx1]{} \left(\frac{2\pi}{9}\right)\omega^3(0)\left(\frac{n}{NA}\right)(\varepsilon-1)^{3/2} \approx V_{excitation}\left(\frac{\varepsilon-1}{4.33}\right)^{3/2}, \qquad (3.10)$$

which corresponds to an ellipsoidal crater of height $2z_T$ and radius $r_T = \omega(0)\sqrt{(\varepsilon-1)/6}$. At high energies per pulse, that is, $\varepsilon \gg 1$, or for focal planes deep to the surface of the tissue, one needs to take into account the decrement in energy as the pulse propagates into the sample and creates a plasma.

3.3.2 Scattering by Brain Tissue

The beam will maintain a focus so long as the elastic scattering length, denoted $\Lambda_{scatter}$, is much greater than the depth of focus, that is,

$$\Lambda_{scatter} \gg z_{confocal}.$$

The scattering length corresponds to the length over which the incident light remains essentially undeflected. For neocortex in living rat, $\Lambda_{scatter} \sim 200$ μm.[41–43] However, for preparations such as the granule cell layer in mouse cerebellum, where the neurons are small and densely packed, the interpretation of preliminary data (Denk and Kleinfeld, unpublished) suggests that $\Lambda_{scatter} \sim z_{confocal}$, and TPLSM is no longer effective.

The argument above suggest that the depth penetration of TPLSM is limited only by the available power. However, the situation is different if structures on the surface of the tissue are labeled in addition to structures at depth. Under this condition, the incident intensity that is required to excite an object at depth can be sufficiently strong to drive two-photon excitation of the same or different molecules near the surface. This can include endogenous fluorophores as well as exogenous labels. Nominally, the maximum distance is found by equating the exponential fall-of in power that occurs with increasing depth against the quadratic increase in intensity as light forms a focus. Further, the numerical aperture decreases with an increase in imaging depth since marginal rays propagate a greater distance than axial rays. These effects result in a practical limit of ~800 μm for the imaging depth with standard 0.8 NA dipping lenses.[43]

3.3.3 Photobleaching and Photodamage by Two-Photon Excitation

The nonlinear excitation profile of TPLSM results in localization of any photodamage, related to bleaching of the fluorophore or otherwise, that may occur. In contrast, single-photon excitation results in photodamage throughout the entire axial extent of the beam. Further, for both single- and two-photon imaging techniques the incident beam can induce heating of the nervous tissue, although this effect may be substantial only when the incident power exceeds ~0.1 W for the near-infrared wavelengths involved in TPLSM.[44]

Increased photobleaching at the focus, possibly driven by third-order or higher nonlinear processes, is a possibility with two-photon excitation. Some experimenters have observed photobleaching rates that scale linearly with absorption[36,45] or scale supralinearly with absorption only at high intensities,[46] while other experimenters have observed the supralinear relation at all intensities.[47,48] Of course, at extremely high peak powers, the laser pulse can cause ionization at the focus that permanently damages the preparation, an effect that we exploit for optical-assisted plasma-mediated ablation.

For imaging through optically thick preparations, TPLSM offers fundamental advantages over single-photon excitation microscopy. For thin preparations, the possibility of increased, but localized photodamage leaves the choice between the single- and two-photon methods unresolved.

3.3.4 Light Source

Pulsed laser light is not monochromatic. A temporally short pulse is composed of a correspondingly broad range of wavelengths. While the exact width will depend on the precise shape of the pulse, the spectral width, $\Delta\lambda$, must scale with the temporal width. The relevant parameters are

$\Delta\lambda \equiv$ Spectral width of pulsed laser light
$\tau_{pulse} \equiv$ Duration of laser pulse
$c \equiv$ Speed of light in air (3.0×10^8 m/s)

The spectra width is thus

$$\Delta\lambda \sim \frac{\lambda_o^2}{c\,\tau_{pulse}}\,. \tag{3.11}$$

For a sufficiently short pulse, the spectral width of the pulse can extend beyond that of the two-photon excitation spectrum for a given fluorescent molecule. In this limit, the excitation efficiency for an excessively short pulse can be lower than for a longer pulse.

A laser with an appropriate pulse width as well as center wavelength, typically between 730 and 1000 nm, must be used in a TPLSM system.[49] Ti:Sapphire-based laser systems have been reported that produce pulses with widths shorter than 10 fs, while commercially available Ti:Sapphire systems that are capable of generating roughly 100 fs duration pulses are readily available and used for our system (see Section 3.4.2). The corresponding full spectral bandwidth is ~10 nm. This width is less than the width of the two-photon absorption band of many relevant dyes (e.g., 80 nm for fluorescein). The pulse is broadened to 200 fs or more at the exit of the objective (Figure 3.27).

The fluorescent light generated by TPLSM is sensitive to fluctuations in the laser power, the center wavelength of the pulse, the pulse width, and the pulse chirp. Recall that this chirp is a shift in frequency between the start and end of a pulse or, equivalently, an evolving phase throughout the pulse. Pulses with different pulse shapes can be characterized by the same width, yet provide different peak powers and thus different excitation strengths, as demonstrated by the examples in Figure 3.3. Additionally, a temporally compact laser pulse incorporates a correspondingly disperse range of laser wavelengths, and these components can be nonuniformly distributed through the pulse envelope, as occurs during chirp (Figure 3.3c).

Ideally, the chirp of the laser pulse should be zero at the focus of the objective so that the spectral composition of the pulse is uniform across the pulse. This results in a minimum pulse width and is usually achieved with external dispersion compensation.[50] While small amounts of chirp are acceptable, heavily chirped pulses can significantly affect two-photon fluorescence efficiencies. For example, the leading edge of a positively chirped pulse can match the two-photon excitation spectrum of a fluorescent dye, while the trailing edge of the pulse corresponds to the slightly red- or Stokes-shifted emission line. Therefore, a molecule can be excited by the leading edge of a pulse, but undergo stimulated two-photon emission with the trailing
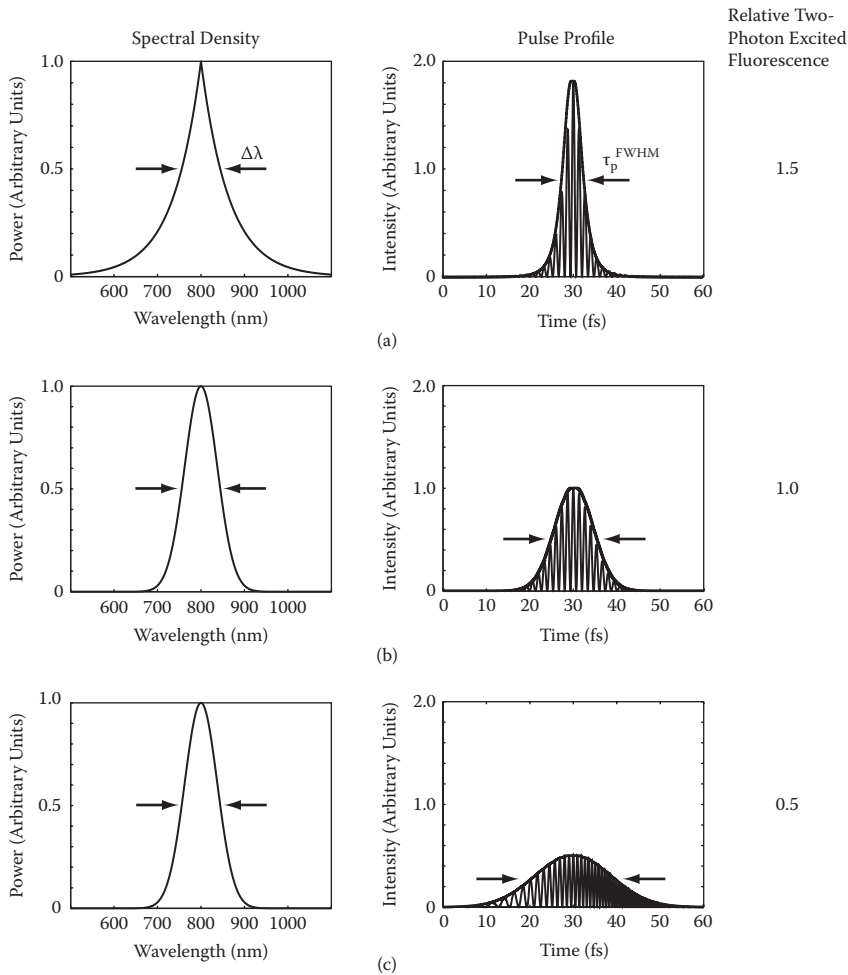
Spectral Density · **Pulse Profile** · Relative Two-Photon Excited Fluorescence

FIGURE 3.3 Pulses with different characteristics can have the same full-width half-maximal pulse-width, indicated by the bar under each pulse. (a) A pulse with a Gaussian envelope. (b) A pulse with a non-Gaussian envelope that has the same pulse width and same integrated area as the pulse in part (a), but has a lower peak power. (c) A pulse in which the constituent frequency components are nonuniformly distributed, that is, chirped. The differences between these pulses have been grossly exaggerated from typical conditions for illustrative purposes.

edge of the pulse before single-photon fluorescence can occur.[51,52] This effect may be responsible for the effect of pulse shape on the rate of photobleaching.[53] With regard to ablation, a pulse that is broadened can lead to the production of heat.

The average output power of the laser can be monitored with a simple photodiode. The center wavelength and the spectral width of the pulse of the laser can be determined with a basic spectrometer. Note that while a fast oscilloscope can be used to display the repetition rate of the laser, even the fastest available oscilloscopes are

currently unable to directly measure the laser pulse width. However, an interferometric autocorrelator can be built to monitor the shape of the pulse (Appendix B). The temporal distribution of wavelengths can only be directly detected by phase measurements with the use of a frequency resolved optical gating or related techniques.[54]

3.3.5 Delivery of Laser Light

The output parameters of a commercial laser system are unlikely to perfectly match the requirements of the microscope. The output beam may not be optimally collimated or may be collimated with a beam diameter that is either too small or too large for use in the microscope. To compensate, the beam profile is calculated along the direction of propagation and can be reshaped using either lenses or curved mirrors.

3.3.5.1 Laser Beam Profile

The laser beam diameter and divergence can be calculated using the paraxial approximation, that is, under the assumption that the intensity along the direction of propagation varies slowly on the scale of the wavelength, and the further assumption that the profile of the intensity follows a Gaussian distribution along the direction that is transverse to that of propagation,[38] with width $\omega(0)$ (Equation 3.1). This is depicted in Figure 3.4 for a divergent laser output that is refocused with an $f = +500$ mm lens; the
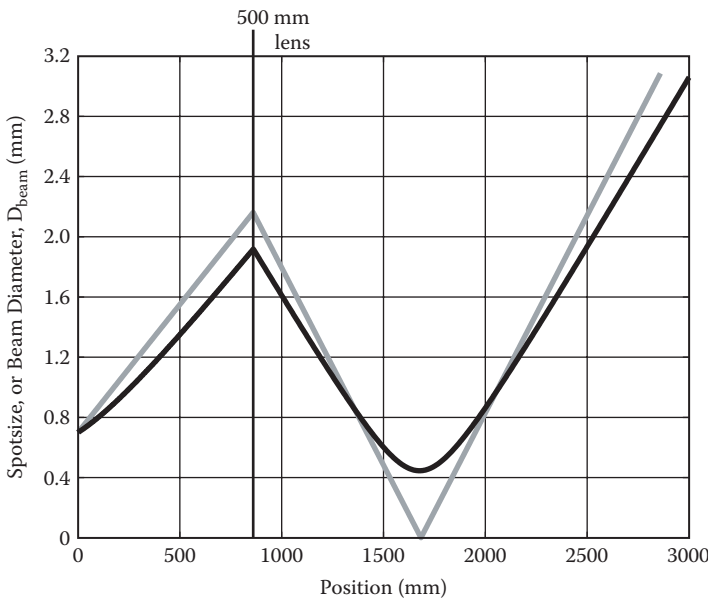
FIGURE 3.4 Calculations of the laser beam diameter, D_{beam}, as a function of distance for a beam with a starting diameter of $D_{beam} = 0.70$ mm and a divergence of 1.7 mrad at a wavelength. These values are typical for the output of a Ti:Sapphire laser. A $f = +500$ mm lens is placed 860 mm from the laser output aperture. The calculation for a Gaussian beam is shown as the dark line, while the geometric optics limit is depicted as the light line.

beam diameter is denoted by D_{beam} and equals the diameter across the points where the intensity falls by a factor of e^{-1}. Superimposed on the Gaussian beam calculation is the calculation for the same system in the geometric optics limit. The result demonstrates that, with the exception of regions close to a focus, the Gaussian beam calculation can be approximated by a geometric optics calculation with modest accuracy.

3.3.5.2 Reshaping the Laser Beam

Several different methods are available to change the divergence and diameter of a laser beam (Figure 3.5). Lenses are simple to align, and the glass will introduce only a small amount dispersion with a 100 fs pulse. Curved metal mirrors do not introduce dispersion under any conditions, and are invariably used with 10-fs pulsed sources. However, metal mirrors must be used off-axis and can thus introduce astigmatism into the laser beam.
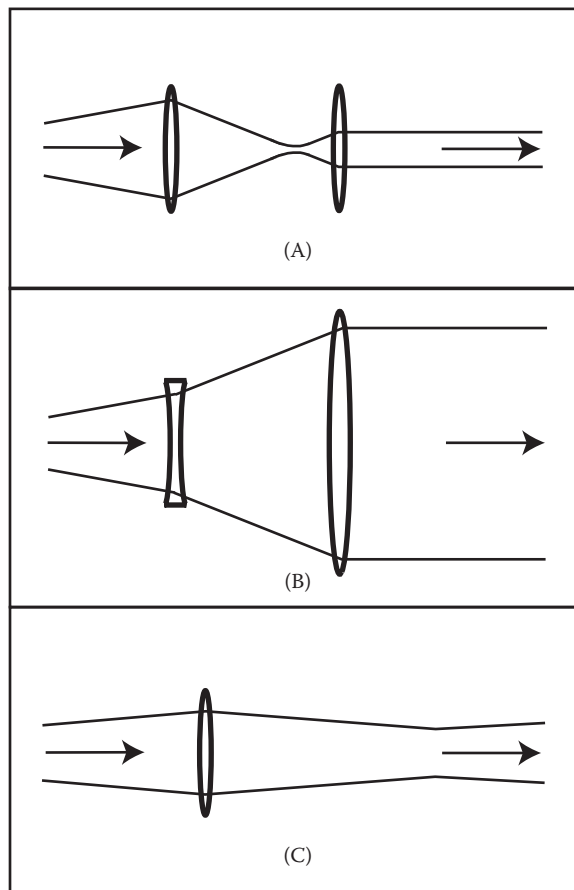

FIGURE 3.5 Four possible methods for reshaping a laser beam. (A) A Keplerian telescope. (B,D) A Galleon telescope. (C) A single, long focal length lens, as used for the calculation of Figure 3.4.

The technical characteristics involved with several lens-based telescope designs refer to the parameters:

$D_{BA} \equiv$ Diameter of the back aperture of the objective
$D_{beam} \equiv$ Diameter the beam at the back aperture

The choices for telescopes includes:

1. A pair of achromatic doublets can be used as a Keplerian telescope (Figure 3.5A). The lens separation should be approximately the sum of the two focal lengths, but the actual location of the telescope along the beam path is flexible. The telescope can easily be adapted to provide different magnifications by choosing different combinations of lenses at the appropriate separation. The disadvantages of this configuration include the need for rails or precision translation stages for precise alignment, and the dispersion produced by the lenses.

2. A pair of lenses, one with positive focal length and the other a negative focal length, can be used as a Galilean telescope (Figure 3.5B). This is critical for the case of amplified laser light that is used with optical ablation, as breakdown of air can occur at the focus of a Keplerian telescope.

3. A single focal length lens can be used to reshape the beam (Figure 3.5C). An achromatic doublet is placed approximately one focal length from the original focus of the laser, which is typically inside the laser cavity. Although the alignment of a single lens is simplified compared to multielement configurations, the collimated beam diameter and placement of the lens are completely determined by the focal length of the lens. As with all lenses, some dispersion is added to the system by this configuration.

4. For complete control of the beam profile with a fixed set of lenses, a four-element double-telescope system should be implemented (Figure 3.6). The laser beam diameter and the divergence can be altered by adjusting the location of two of the four elements. The deficit of this system is additional dispersion. Note that, in principle, a three-element system provides sufficient degrees of freedom but is somewhat more difficult to adjust.

5. In general, the laser beam should be collimated to minimize the spherical aberrations of the objective. As a practical matter, it may be necessary to introduce a slight convergence or divergence to the beam, as most lenses are designed to minimize spherical aberrations for visible (400 to 600 nm) light rather than near-infrared (700 to 1000 nm) light. The final size of the beam represents a compromise between resolution, which increases as the back aperture of the objective is increasingly filled, and throughput, which is maximal when the back aperture is underfilled. This trade-off is illustrated in terms of the normalized beam diameter, D_{beam}/D_{BA} (Figure 3.7); $D_{BA} \approx 6.6$ mm with the back-aperture located 35 mm from the back shoulder for the 40-times magnification, 0.8 NA dipping objective (no. 440095, Zeiss).
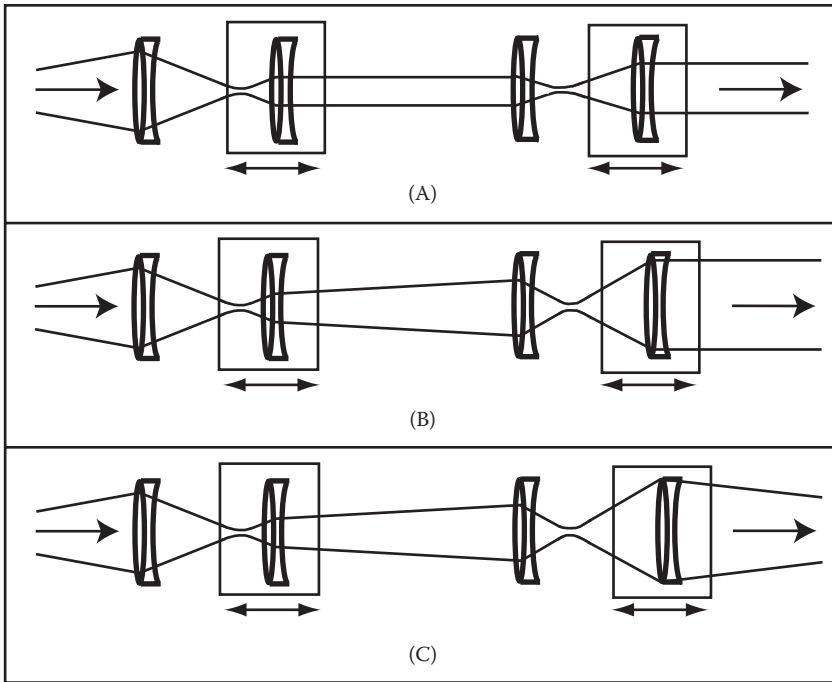
FIGURE 3.6   Ray diagrams for a dual telescope system with four lenses. The output beam diameter and divergence can be completely controlled by translating two of the four lenses. For illustration, we take the input beam to be divergent. (A) A collimated, smaller diameter output. (B) A collimated, larger diameter output. (C) A converging, larger diameter output.

3.3.6   DESIGN OF A SCAN SYSTEM

We consider in detail the manipulation of the path of the laser beam as a means to scan a focused spot across the preparation. The essential idea is that the objective converts the incident angle of a collimated beam into the position of a diffraction limited spot on the focal plane (Figure 3.8A). The focused laser spot can be moved across a stationary preparation by changing the angle of the incident beam. In order to change the angle without having to physically move the source, one uses a system of mirrors and auxiliary lenses according to one of two schemes.[34] The first method involves a standard 160 mm tube length objective, that is, a lens optimized for an image plane at 160 mm from the rear focal plane of the objective, in conjunction with a rotating mirror and a scan lens to deflect the rotated light back into the beam path (Figure 3.8B). A disadvantage to this configuration for TPLSM is that the incoming light to the objective is convergent, rather than parallel. This can lead to astigmatism in the focused beam if a dichroic mirror is placed directly behind the objective, as is optimal for collection of emitted light in TPLSM.[7]

An alternative scheme for the scan system is to use an infinity-corrected objective (i.e., one that is optimized for an image in the conjugate plane), together with a
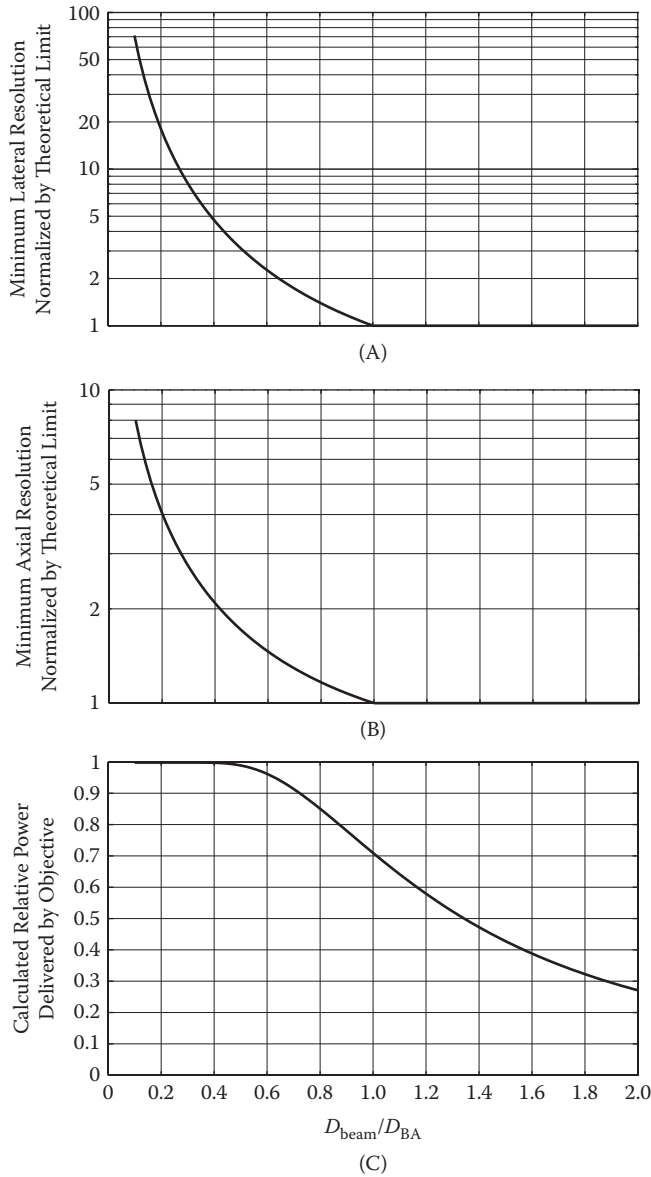
FIGURE 3.7 The trade-off between power throughput and optical resolution as a function of the size of an incident Gaussian beam, normalized as in units of Dbeam over DBA. (A) elative power versus normalized radius. (B) Lateral resolution versus normalized radius. (C) Axial resolution versus normalized radius.

rotating mirror and a tube lens as well as a scan lens (Figure 3.8C). In this configuration, the two auxiliary lenses serve to translate the angular deflection of the mirror into an incident angle at the objective, while allowing both the input to the mirror, and the input to the objective to be collimated. This is the configuration used in our
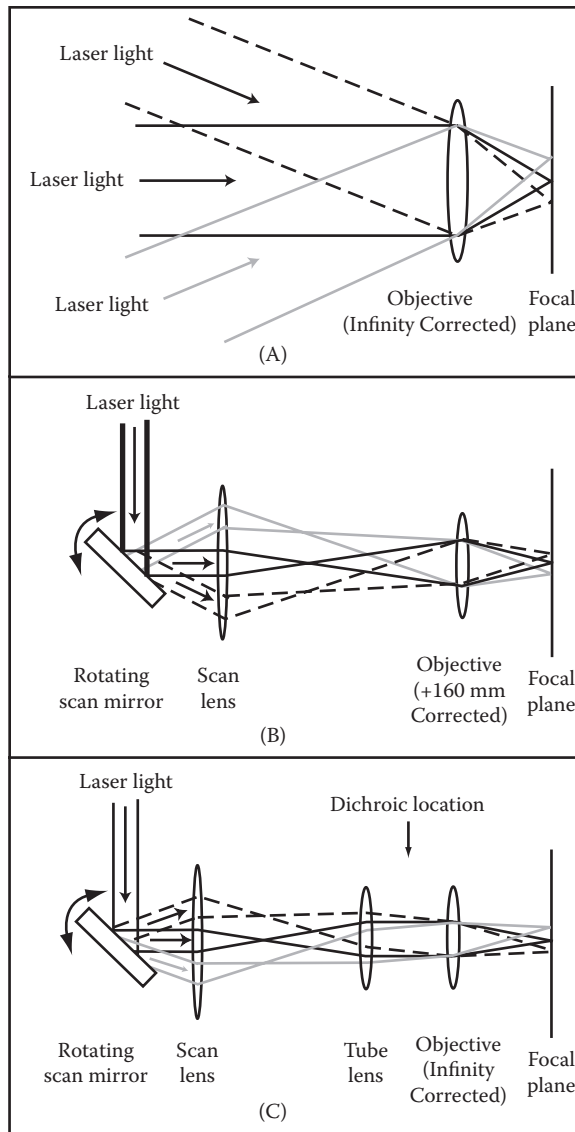
FIGURE 3.8 Illustration of different configurations for laser scanning. (A) A scanning system with only an objective. The collimated laser source must be physically moved and rotated behind an infinity-corrected objective. (B) A scanning system with a single intermediate lens, that is, the scan lens, in addition to the objective. The objective is taken as optimized for a 160-mm image distance. The rotating mirror is imaged onto the back aperture of the objective. Note that the light is convergent behind the objective. (C) A scanning system with two intermediate lenses, that is, the scan lens and the tube lens, in addition to the objective. The objective is taken as optimized for an infinite image distance. A scan lens and tube lens are placed between a rotating scan mirror and an infinity-corrected objective. The mirror surface is imaged onto the back aperture of the objective and the light between the objective and the tube lens is collimated and thus suitable for the placement of a dichroic mirror.
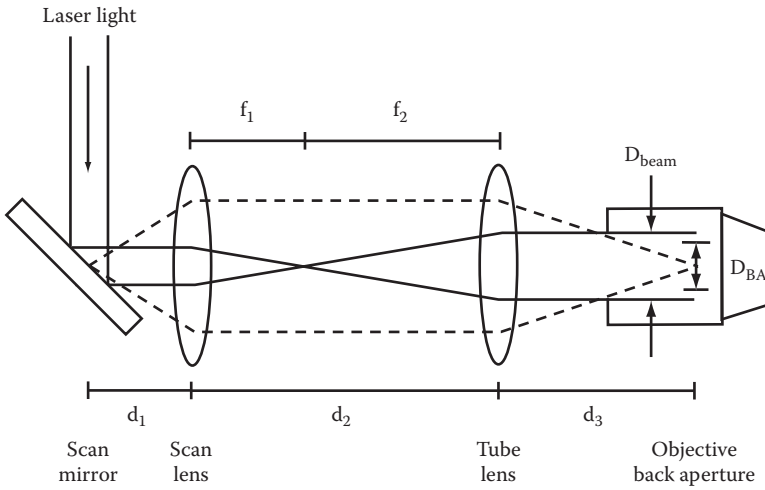
FIGURE 3.9   The alignment of optics in a scanning system consisting of an objective, tube lens, and scan lens. The actual laser pathway is indicated by the solid lines. The dashed lines depicts the imaging condition between the center of the scan mirror and the center of the back aperture of the objective. The laser path is magnified to just overfill the back aperture, and the imaging condition (see text) prevents motion of the laser spot at the back aperture as the laser beam is scanned.

system, and which will now be described in greater detail (Figure 3.9). The relevant additional variables are

$f_1 \equiv$ Focal length of scan lens
$f_2 \equiv$ Focal length of tube lens
$d_1 \equiv$ Distance between the scan mirror pivot point and the scan lens
$d_2 \equiv$ Distance between the scan lens and the tube lens
$d_3 \equiv$ Distance between the tube lens and the back aperture of the objective
$D_{SM} \equiv$ Effective diameter of the scan mirror
$d_{SM} \equiv$ Distance between a pair of scan mirrors

The issue of 1D versus 2D scanning can be separated from the issue of constraining the optics in the beam path. Thus, for clarity, we focus first on a 1D scan system.

3.3.6.1 Constraints on Axial Distances and Optical Apertures

We consider the optimal alignment and layout of optics, with reference to Figure 3.9, for TPLSM. The constraints are:

1. Infinity-corrected objectives require the incident light to be collimated at the back aperture of the objective, which is a plane specified by the manufacturer that may lie deep within the lens. If the input to the scan system is a

collimated laser beam, then the scan lens and tube lens must be configured as a telescope. Therefore, their separation is given by

$$d_2 = f_1 + f_2. \tag{3.12}$$

2. The pivot point of the scan mirror should be imaged to the center of the back aperture of the objective to minimize motion (spatial deviations) of the laser path at the back aperture plane. This imaging condition is satisfied by

$$d_1 = \frac{(f_1)^2}{f_2} + f_1 - d_3 \left(\frac{f_1}{f_2} \right)^2. \tag{3.13}$$

This condition serves to maintain constant laser power through the back aperture of the objective as the scan mirror is rotated. It ensures that the intensity at the focus does not change as the mirror rotates. A graph of the required separation, d_1, as a function of the separation, d_2, for six different choices of scan lens focal lengths and a tube lens with a focal length of $f_2 = +160$ mm is shown in Figure 3.10.

3. The incident laser beam should slightly overfill the back aperture of the objective in order to utilize its full NA, that is,

$$D_{\text{beam}} > D_{\text{BA}}. \tag{3.14}$$

This leads to the highest resolution for a given objective.
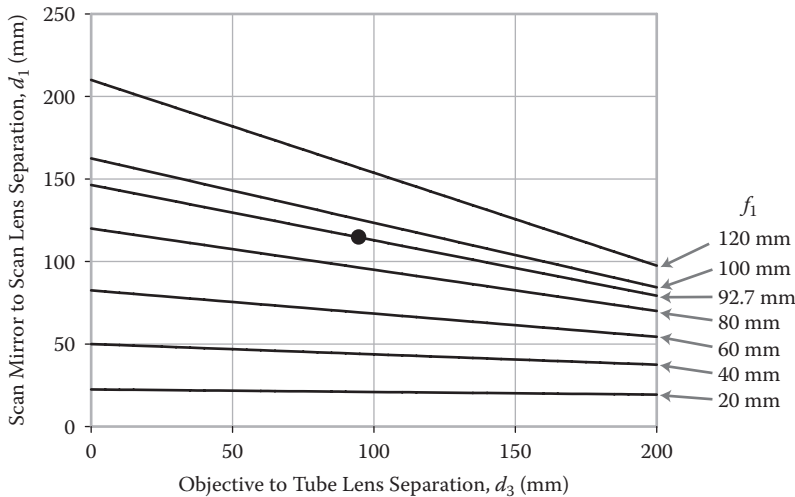

FIGURE 3.10 The calculated scan mirror to scan lens separation distance, d_1, as a function of the objective to tube lens separation distance, d_3. The calculation is shown for several choices of scan lens focal lengths, f_1. The focal length of the tube lens is assumed to be $f_2 = +160$ mm. The dot marks the actual values, $d_3 = 95$ mm and $f_1 = +92.7$ mm, used in our system.

4. Typical fast scan mirrors are only 3 mm in dimension. The simultaneous requirements that the beam should underfill the scan mirrors as a means to avoid losses due to diffraction, yet slightly overfill the back aperture of the objective as a means to maximize the spatial resolution at the focus, constitute a magnification constraint on the scan system. The required magnification, denoted m, is given by

$$\left| m \right| \equiv \frac{D_{BA}}{D_{SM}} \simeq 2\,\tfrac{1}{2}\ \text{to}\ 7 \tag{3.15}$$

where the numerical values are span the range of values appropriate for the back aperture of a standard 40-times magnification dipping lens ($D_{BA} \approx 7$ mm) through a wide-field 20-times magnification dipping lens ($D_{BA} \approx 21$ mm). The scan lens should be a lens with a small f-number—that is, a ratio of focal length to clear aperture—that is well corrected for spherical and off-axis aberrations. These conditions are satisfied with an achromatic doublet with an f-number of 2. Precision scan lenses, as well as stereoscope objectives, are well corrected for off-axis aberrations and thus beneficial for applications involving large scan angles.

5. For the case of a system in which a trinocular with a standard, $f_2 = +160$ mm tube lens is used in the scan system, the required focal length of the scan lens is determined by a second constraint on the magnification, that is, $f_1 \equiv f_2/|m|$, for which the standard focal lengths of 63.5, 50.8, 38.1, 31.8, or 25.4 mm are appropriate. For the case in which a custom tube lens is used, a convenient choice in terms of availability is $f_2 = 200$ mm in conjunction with scan lenses of $f_1 = 76.2, 63.5, 50.8, 38.1, 31.8,$ or 25.4 mm; these span the range m = 2.7 to 7.8. The theoretical two-photon intensity profile for different filling rations D_{beam}/D_{BA} is estimated by modeling this system with geometric optics (Figure 3.11).

6. The above constraints (Equations 3.12 to 3.15) leave a single degree of freedom in the design of the scan system. For a given separation distance between the tube lens and the objective, d_3, the imaging constraint determines the scan-lens-to-scan-mirror separation distance, d_1, or vice versa (Figure 3.10). In practice, many objectives are designed to be corrected for chromatic aberration at a fixed value of d_3. For Zeiss objectives, this is

$$d_3 \cong 95\ \text{mm}; \tag{3.16}$$

other manufactures may have slightly different values. In practice, d_3 is also constrained by the physical size of the detector assembly.

3.3.6.2   Two-Dimensional Scanning

A distortion-free, two-dimensional scan is obtained with two scan mirrors and the use of a unity magnification telescope optics between the scan mirrors to ensure that the centers of both mirrors and the objective back aperture are all conjugate planes
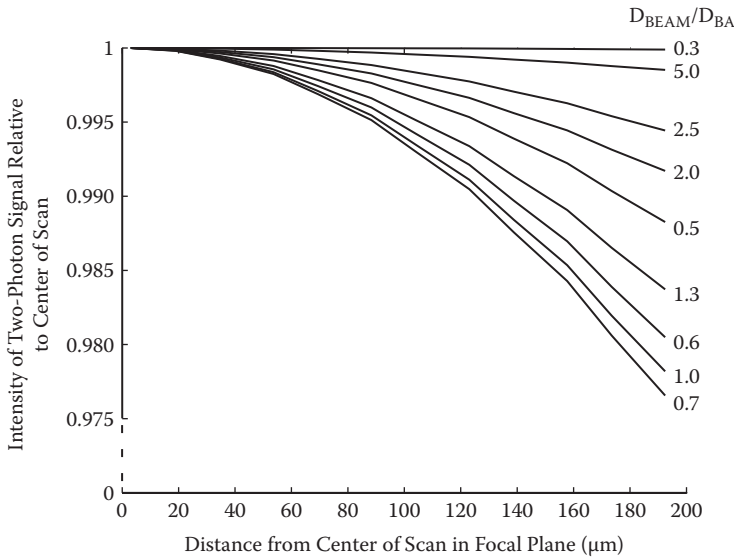
FIGURE 3.11 Theoretical calculation of the spatial inhomogeneity of the squared power, which corresponds to the two-photon excitation rate, due to the lateral motion of the scanned laser spot at the back aperture of the objective. The calculation was carried out in the geometric optics limit with the assumption of a Gaussian transverse beam profile.

of one another. The addition of the intermediary optics is conceptually straightforward and was employed in commercial instruments, that is, the Biorad MRC series.

A simpler 2D scan configuration can be used that utilizes no intermediary optics if the separation between the scan mirrors can be made small compared to focal length of the scan lens, that is,

$$f_1 \gg d_{SM}. \tag{3.17}$$

The conjugate plane of the back aperture is placed halfway between the two scan mirrors. The small deviation from the exact imaging conditions results principally in a slight lateral motion of the beam at the back aperture of the objective while the beam is scanned. This motion results in increased clipping (i.e., vignetting) of the beam at larger scan angles. The excitation intensity will therefore be lower at the edges of the scan than at its center (Figure 3.11).

3.3.7 FLUORESCENT LIGHT DETECTION

The fluorescent signal generated in the illuminated region of the preparation is incoherent and is emitted over the entire 4π solid angle. A portion of the signal is collected in the backward direction by the objective, deflected by a dichroic beamsplitting mirror, and focused onto a photomultiplier tube (PMT) (Figure 3.12). Filters and additional dichroic mirrors and detectors can be used to further isolate
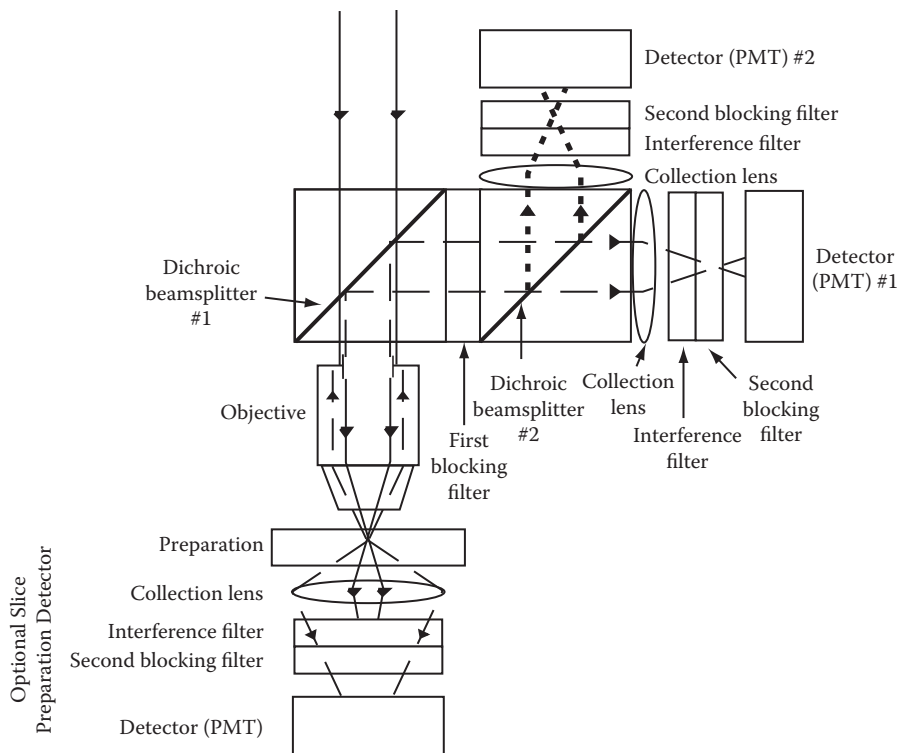
FIGURE 3.12   Schematic of the detection configuration for two-photon excited fluorescence. The excitation laser light is depicted as a solid line, while the fluorescent signals are shown as dashed and dotted lines. The collection system shown below the sample stage can be added for samples that are not too optically thick, such as brain slice.

the fluorescent signal and, if required, separate different fluorescent signals according to wavelength. For preparations that are not too optically thick (e.g., slice or cell culture), an additional detector can be placed beneath the preparation to collect the signal emitted in the forward direction[55] (Figure 3.12).

3.3.7.1   Placement of Detector Assembly

The detector assembly should be placed directly above the objective. The two main considerations in this choice of detector position are:

1. Collection efficiency is increased by placing the collection assembly directly above the objective. Although light that is emitted from the focal plane of the infinity-corrected objective should ideally be collimated as it returns through the back aperture, the actual fluorescence will diverge due to scattering and diffraction. In particular, it is mainly the scattered light that will miss the clear aperture of the tube lens. The unscattered light collected by the objective will almost exactly retrace the beam path of the excitation laser. Therefore, the placement of the detector assembly as close

to the objective as possible should result in improvements for more strongly scattering preparations.

2. Fluorescent light collected from an infinity-corrected objective will be nearly collimated just above the objective. Placing the dichroic mirror in the path at this point, rather than at a location where the beam is diverging, reduces the sensitivity of the signal to local defects on the dichroic mirror.

3.3.7.2 Constraints for Detection Elements

The backward collection pathway is shown in Figure 3.13 with the second dichroic mirror and PMT pathway eliminated for clarity. We note the following definitions:

$l_1 \equiv$ Distance between collection lens and back aperture of the objective
$l_2 \equiv$ Distance between active surface of the detector and collection lens
$D_{PMT} \equiv$ Effective diameter of the detector active surface
$f_{CL} \equiv$ Focal length of the collection lens
$D_{CL} \equiv$ Clear aperture of the collection lens

The following conditions should be maintained for the choice and placement of collection optics:

1. The back aperture of the objective should be imaged onto the active surface of the PMT to minimize motion of the fluorescent signal on the detection surface. This imaging condition is given by

$$l_2 = \frac{l_1 f_{CL}}{l_1 - f_{CL}} \tag{3.18}$$

and is graphed in Figure 3.14 for five choices of collection lens focal lengths, f_{CL}.
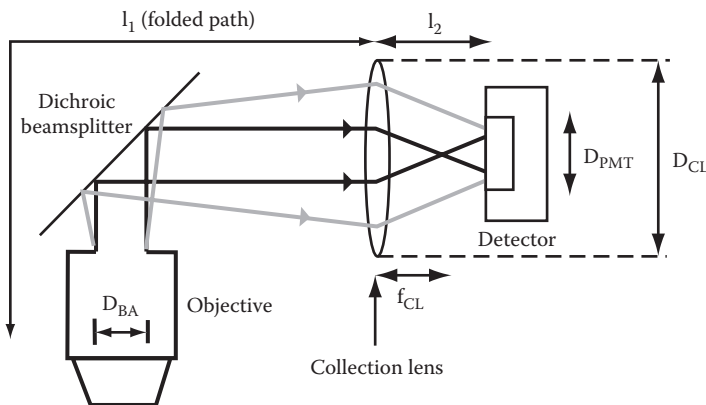

FIGURE 3.13 Placement and separations of detector elements for two-photon excited fluorescence. Unscattered fluorescent light is depicted as a dark line, while scattered fluorescent light is depicted as a gray line.
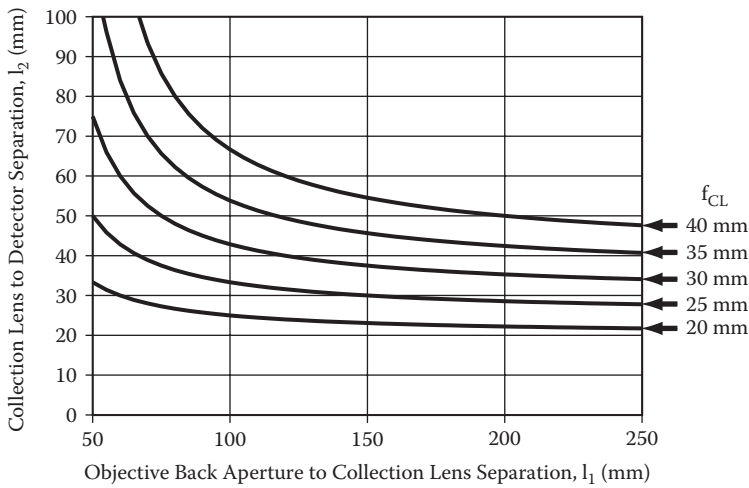
FIGURE 3.14 Graph of the imaging constraint for the distance between the detector and the back aperture of the objective for five choices of focal length for the collection lens.

2. The collection lens should have a large clear aperture to maximize collection of scattered light, some of which diverges as it exits the back aperture of the objective. In practice, physical constraints of the detector assembly (described in detail later), limit the clear aperture to

$$D_{CL} \approx 30 \text{ mm} . \tag{3.19}$$

3. The separation between the collection lens and the objective should be minimized to within physical constraints. This also serves to increase the collection efficiency of the scattered light. As a maximal limit, we arbitrarily choose a distance at which a clear aperture is at least half of the empirically determined maximal divergent spot size from the back of a typical objective. For example, this corresponds to a half-angle spread of 11° from the $D_{BA} = 7$ mm back aperture of a 40 magnification objective and implies that the collection lens, with a clear aperture of $D_{CL} = 30$ mm, should be placed at

$$l_1 \cong 130 \text{ mm} . \tag{3.20}$$

4. The focal length of the collection lens should be as short as possible. This, in combination with the imaging constraint of Equation 3.18, ensures that the image of the back aperture is minified to fit onto the smaller active area of the PMT. The magnification is given by

$$|m| = \frac{f_{CL}}{l_1 - f_{CL}} . \tag{3.21}$$

The active area of the PMT described in this chapter is 4 mm. The objective back apertures range up to 12 mm in diameter. Therefore, the magnification requirement for the described system is $|m| = 1/3$. Together with $l_1 = 130$ mm (Equation 3.21), we have

$$f_{CL} = 32.5 \text{ mm.} \tag{3.22}$$

In many imaging applications, aberrations and misalignment of optical elements distorts the spatial distribution of the collected light. This directly affects the resolution of the final image. In laser scanning microscopy, the final image is produced as a time series of collected light intensities. All of the light collected during a given time interval contributes equally to the intensity value of the corresponding spatial pixel, at least insofar as the efficiency of the detector is spatially uniform. Thus, it is more important that a consistently large portion of the fluorescent light is collected at the detector than to minimize aberrations in the collection optics.

3.3.7.3 Emitted Photon Yield per Laser Pulse

The constraints on the choice of detection electronics depends on the number of fluorescent photons emitted per incident laser pulse and on the efficiency of converting those photons into photoelectrons at the detector. For this analysis, the additional relevant parameters are

$n_{pulse}^{incident} \equiv$ Number of incident photons per laser pulse

$n_{pulse}^{collect} \equiv$ Number of emitted photons collected per pulse

$P_{pulse}^{incident} \equiv$ Peak power of incident laser pulses

$\Phi_{pulse}^{incident} \equiv$ Flux of incident photons

$\Gamma \equiv$ Repetition rate of laser pulses

$\tau_{pulse} \equiv$ Width of laser pulse

$\beta^2 \equiv$ Relative variance of laser pulse intensity, $\left\langle (\Phi_{pulse}^{incident})^2 \right\rangle / \left\langle \Phi_{pulse}^{incident} \right\rangle^2$

$N_{molecules} \equiv$ Number of molecules in focal excitation volume

$\xi_{obj} \equiv$ Collection efficiency of objective

$h \equiv$ Planck's constant (6.6×10^{-34} Js)

$N_a \equiv$ Avogadro's number (6.0×10^{23} molecules/mole)

The number of photons per laser pulse is

$$n_{pulse}^{incident} = \frac{\lambda_o}{hc} \frac{P_{average}^{incident}}{\Gamma} . \tag{3.23}$$

For $P_{average}^{incident} = 10$ mW, below the ~ 30 mW saturation of organic fluorophores,[56] with $\lambda_0 = 800$ nm and $\Gamma = 76$ MHz, we find

$$n_{pulse}^{incident} = 5 \times 10^8 \text{ photons/pulse.}$$

The incident flux is

$$\Phi_{pulse}^{incident} = \frac{\lambda_o}{hc} \frac{P_{average}^{incident}}{\pi\ \omega^2(0)\ \tau_{pulse}\Gamma} \tag{3.24}$$

which, for NA = 0.8 so that $\omega(0) \approx 0.25$ µm (Equation 3.1) and the typical value of $\tau_{pulse} = 250$ fs for width measured at the objective (Section 3.5.2), yields $\Phi_{pulse}^{incident} \approx 1.0 \times 10^{34}$ photons/m^{2}s. The number of emitted fluorescent photons captured by the objective is

$$n_{pulse}^{collect} = \xi_{obj}\ \tfrac{1}{2}\ \sigma_{dye}\ \beta^2 \left\langle \Phi_{pulse}^{incident} \right\rangle^2 \tau_{pulse} N_{molecules} \tag{3.25}$$

where the $\tfrac{1}{2}$ represents the conversion of two incident photons to one fluorescent photon,

$$N_{molecules} \simeq \left[dye \right] N_a\ V_{excitation} \tag{3.26}$$

and the epifluorescent collection efficiency is

$$\xi_{obj} = \frac{1}{4\pi} \int_0^{\sin^{-1}\frac{NA}{n}} \int_0^{2\pi} \sin\theta\ d\theta\ d\phi = \frac{1}{2}\left[1 - \sqrt{1 - \left(\frac{NA}{n}\right)^2} \right] \xrightarrow{NA \ll n} \frac{1}{4}\left(\frac{NA}{n}\right)^2 . \tag{3.27}$$

The typical dye concentrations varies from 10 to 50 µM (average of 20 µM) for the intracellular calcium indicator Calcium Green 1[57], from 10 to 90 µM (average of 40 µM) for the intracellular calcium indicator Fura-2[58,] and up to 150 µm for blood serum labeled with fluorescein conjugated to dextran.[3] For the choice [dye] = 20 µM and the previous choice of NA = 0.80, for which $V_{excitation} \cong 1.5 \times 10^{-16}$ L (Equation 3.3) and $\xi_{obj} = 0.10$ (Equation 3.27), we estimate $N_{molecules} \approx 1800$. The normalized variance for a transform limited pulse is $\beta^2 = 0.6$[7]. The cross-section for Calcium Green at $\lambda_o = 800$ nm is $\sigma_{dye} = 20$ GM $= 20 \times 10^{-58}$ m^{4}s/photon, for which we estimate

$$n_{pulse}^{collect} \approx 3 \text{ photons/pulse.}$$

As discussed under "Realization" (Section 3.4.6.2), losses from the dichroic and band-pass filters used in the separation of the incident and emitted light and inefficiencies of the photodetector lead to another order of magnitude decrement in the transformation from collected photons to integrated photoelectrons. A final point is that while the excitation rate $\tfrac{1}{2}\ \sigma_{dye}\ \beta^2 \left\langle \Phi_{pulse}^{incident} \right\rangle^2 \tau_{pulse} N_{molecules}$ is independent of the NA of the objective,[7] the number of collected photons increases with increasing numerical aperture (Equation 3.25).

3.4 REALIZATION

3.4.1 OPTICAL AND MECHANICAL

Our system is laid out on a 4′ × 8′ × 1′ air table, which provides room for the lasers, ancillary optics, an interferometric autocorrelator, and a repetition rate doubler (Figure 3.15).
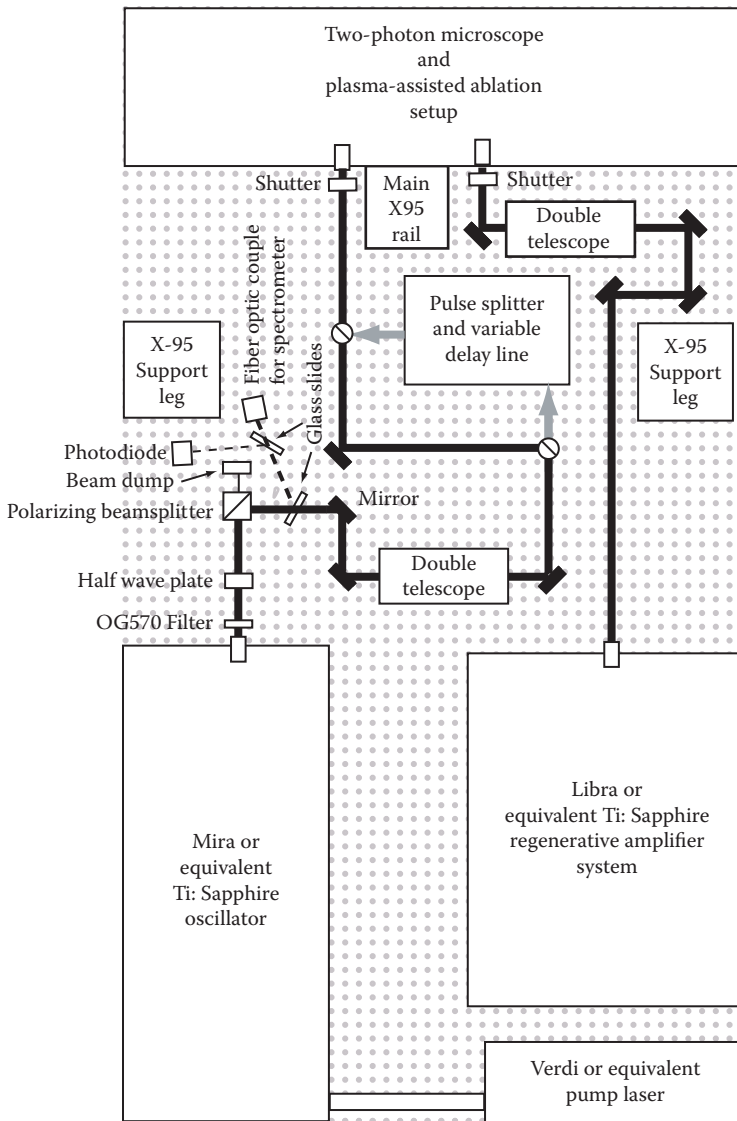
FIGURE 3.15 Schematic diagram of the layout on an optical table for delivery of laser light to our two-photon laser scanning microscope with amplified ultrashort pulses for photon-assisted plasma-mediated ablation. The main beam path is depicted by the thick dark line. The beam path through the pulse splitter and delay line, used for the optical autocorrelator, is depicted by the thick gray lines. The beam path to the additional experimental setup is depicted by the thin dark line. The beam path to the two-photon spectrometer is depicted by the thin gray line. The dashed line behind the first polarizing beamsplitter represents the path for the horizontally polarized component of the beam that is used to monitor the output power and wavelength of the laser, as well as dissipate excess power. Circles with diagonal lines represent protected silver mirrors in flipper mounts. Rectangles at 45° represent protected silver mirrors in standard mirror mounts. The dimensions of the table are 4′ by 8′.

Room for dispersion compensation optics, should they be required, is also available. Wherever possible, standard, commercially available optics and electronics were used to maximize the reproducibility of the system; these are summarized in Appendix A. Various adapters were fabricated to combine parts of noncompatible design. Machine drawings of these adapters are available by contacting the senior author. Lastly, ancillary electronics are supported by a hanging shelf above the air table.

3.4.2 Laser Systems

The most versatile source for TPLSM remains the Ti:Sapphire oscillator. The output of these lasers peaks at $\lambda_o = 800$ nm but can be equipped with broadband mirror sets that permit the output to be tuned from below 750 to over 1000 µm. The pulses that emanate from the oscillator are τ_{pulse} ~100 fs in width, can be compensated to be free of chirp, and are delivered at a repetition rate of Γ ~80 MHz. The time between pulses, Γ^{-1} ~13 ns, is long compared with typical fluorescent lifetimes of 2 to 5 ns.

There are basically two options for obtaining a system:

1. A "two-box" version uses a separate pump laser and oscillator. The diode pump laser can deliver up to 20 W of pump power at a wavelength of $\lambda = 532$ nm, close to the maximum thermal limit of the Ti:Sapphire crystal. The maximum average output power of such a laser is approximately 3 W at $\lambda_o = 800$ nm, or upward of 100 times the saturation power for typical dyes.[7] This allows for over two orders of magnitude of loss due to scattering as one probes deep into brain tissue. These laser are relatively robust.
2. A "one-box" contains in integrated pump laser and oscillator, together with automated tuning protocols. These system are simple to use and permit relatively fast shifting of wavelengths with uninterrupted lasing. The potential drawback of "one-box" systems is that the automated tuning circuitry holds the beam path at the same location in the Ti:Sapphire crystal, which results in laser-induced damage and a drop in output power over time compared to "two-box" systems.

The laser source for plasma-mediated ablation only needs to operate at a single wavelength. These systems need to supply upward of 10^3 times more energy per pulse than the lasers used for imaging, which implies that they will have relatively low repetition rates. Commercial systems use pulses from a standard Ti:Sapphire oscillator as a seed, and amplify these pulses in a regenerative scheme that involves pulse stretching and compression. While our initial system was based on the design of Murnane,[59] we have had excellent success with the "one box" Libra from Coherent Inc., which has a repetition rate of 5 kHz. Fiber-based systems, and long-baseline or cavity-dumped Ti:Sapphire oscillators, may be viable alternative sources.

3.4.3 Path from Lasers to Microscope

The delivery pathway of the laser light from the source to the scanners is depicted in Figure 3.16. A colored glass filter, type OG590, is placed immediately after the
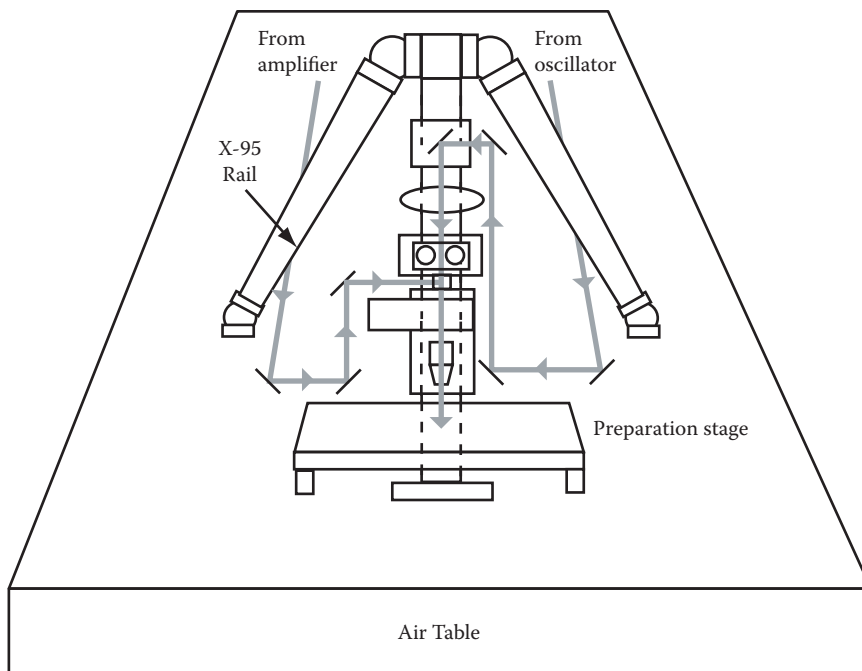
FIGURE 3.16 Illustration of the physical superstructure of the two-photon laser scanning microscope. The tripod is constructed of X-95 rail; the front leg forms the optical rail of the microscope and the side legs act as supports. The incident laser paths are shown in gray.

laser output port as a means to attenuate any residual $\lambda = 532$ nm pump light along the beam path. The output of the Ti:Sapphire laser is horizontally polarized, and thus the intensity of the laser output may be controlled by manipulating the polarization state. The polarization angle is rotated by a zero-order half-wave plate and a polarizing beamsplitter or a Glan-Thompson polarizer, is used to separate the polarized light into its horizontal, or P, and vertical, or S, components. The vertical component, which has a slightly higher reflectance by metal mirror surfaces that are mounted on the table top and positioned at an angle of 45° relative to the beam path, is deflected toward the microscope. Rotation of the output polarization from horizontal to vertical, via rotation of the half-wave plate, increases the deflection to the microscope according to the cosine of the angle. Intensity control on the millisecond time-scale can be achieved using a Pockels cell to rotate the angle of the beam, rather than a mounted half-wave plate.

For beam diagnostics, a glass slide that is positioned at 45° relative to the beam is used to pick off roughly 8% of the beam power and deflects it to a PC-based spectrometer via a fiber-optic cable (Figure 3.15). An additional glass slide is used to pick off an additional roughly 8% of the beam power and deflects it to a photodiode as a relative measure of the intensity of the laser output. Independent of which polarization is monitored by the photodiode, the pick off should be located downstream of the intensity control mechanism(s) but upstream of the shutter.

Typically, a two-lens telescope is used to reshape the laser beam for input to the microscope as required. For example, the output of the Mira 900F oscillator has a 1.7 milliradian (full angle) divergence and an initial beam diameter of $D_{\text{beam}} = 0.7$ mm. This is reshaped to a beam diameter equal to that of the scan mirrors, that is, $D_{\text{SM}} = 3$ mm, with a $f = +25$ and $+100$ mm pair of achromats.

A mechanical shutter is placed in the beam path just before the beam is deflected upward by a periscope toward the scan mirrors (Figure 3.15). The shutter position is computer controlled, and for safety reasons, its default position in the absence of electrical power blocks the beam from the scanners.

As a practical issue, for purposes of alignment, we use iris diaphragms as variable apertures to define the height and position of the beam. In this scheme, two well-separated mirrors are followed by two well-separated diaphragms, with the first diaphragm close to the last mirror for ease of alignment of the beam. Unless otherwise stated, all mirrors have a flat, protected-silver surface and are held in standard kinematic mounts. Lastly, safety precautions must be maintained in the use of laser light for TPLSM. Thus black anodized metal shields are used to surround the scanners and some optics that are located near normal eye level.

3.4.4 Path along Microscope: Two-Photon Excitation

The microscope is built as a tripod with X-95 optical rail (Figure 3.16). One leg serves as an optical bench, and the other two serve as supports. A customized adapter atop the tripod serves to connect the legs. A pair of mirrors mounted at 45° is used as a periscope to steer the beam to the height of the scan mirrors. The top periscope mirror mount is connected horizontally to the main X-95 rail and angled at 45°. The laser light deflected from the top periscope mirror travels horizontally to the alignment mirror, and then to the two scan mirrors. The laser then travels downward through the scan lens, the tube lens, the polarizing beamsplitter, and the dichroic beamsplitter, before being focused by the objective onto the preparation (Figure 3.17).

There are five main attachments to the main X-95 rail (Figure 3.17). At the top, two carriages are attached; one in front, and one in back. The front carriage holds the scanners and an alignment mirror, and the back carriage holds the top half of the periscope. The next attachment is the scan lens mount. A 100%/0% switching trinocular headstage, which provides the eyepieces for visual inspection of the preparation and holds the tube lens, is mounted on a separate X-95 carriage below the scan lens. The underside of the attachment for the trinocular tube also holds a polarizing beamsplitter for bringing in the amplified pulse laser source. The bottom attachment is a modular focusing unit, to which both the detector assembly and the objective holder are mounted. Lastly, the sample stage allows for "x" and "y" translation of the preparation and sits directly on the air table.

Optical scanner. The back X-95 carriage holds the top mirror of the periscope for the oscillator. An "L" bracket attaches to the mirror mount and holds it in the appropriate orientation (Figure 3.17). The front X-95 carriage is connected to a rod assembly that holds both the scanners and an alignment mirror (Figure 3.18). The alignment mirror is located at the orthogonal intersection point of the planes defined by the periscope mirrors and the first scan mirror. The scanners are mounted in a
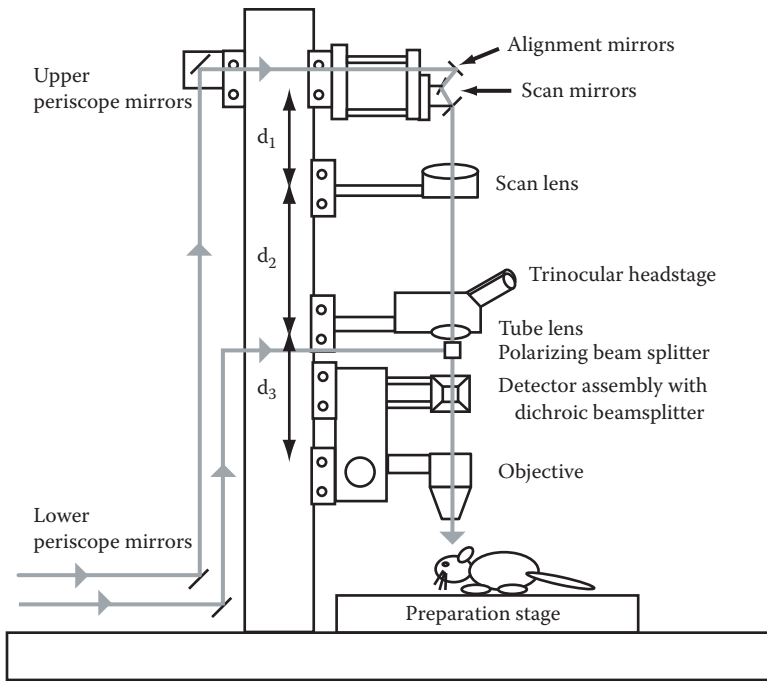
FIGURE 3.17 The main attachments to the main X-95 rail in the two-photon laser scanning microscope. The laser pathway from one of the periscopes to the objective along the optical rail that forms the microscope includes the alignment mirror, the scan mirrors, the scan lens, the tube lens, the polarizing beamsplitter, and the detector assembly. The pathway from the other periscope to the objective along the optical rail that forms the microscope includes only the polarizing beamsplitter. The collection optics for the fluorescent light are not shown. The values of the separation distances for our system are $d_1 = 114.5$ mm, $d_2 = 252.7$ mm, and $d_3 = 95$ mm.

small, orthogonally positioned mirror assembly that is a manufacturer's accessory to the scanners. The mirror assembly is attached to a custom-designed, water-jacketed base that in turn is attached to the rod assembly; water cooling is only necessary for large scan angles at the highest speeds, an atypical situation. The rod assembly itself consists of seven posts (i.e., 2 of 8", 4 of 6", and 1 of 4") and seven cross-post adapters.

Scan lens. The scan lens is a 1.0-times magnification plan dissection lens (Leica). It is held and centered on a custom-designed mount and attached to the main X-95 carriage (Figure 3.17). A major consideration for the design of the scan lens holder is mechanical stability, and thus our mount is reinforced with diagonal cross-bracing.

Headstage. The headstage is an upright trinocular (Zeiss) in which the phototube pathway is used as the laser beam pathway (Figure 3.17). The headstage contains a 100%/0% beam switcher that is used to change between visual inspection with the binocular and laser scanning microscopy. The trinocular contains a $f_2 = +160$ mm tube lens that is used as the second lens of the scan system telescope. The trinocular is
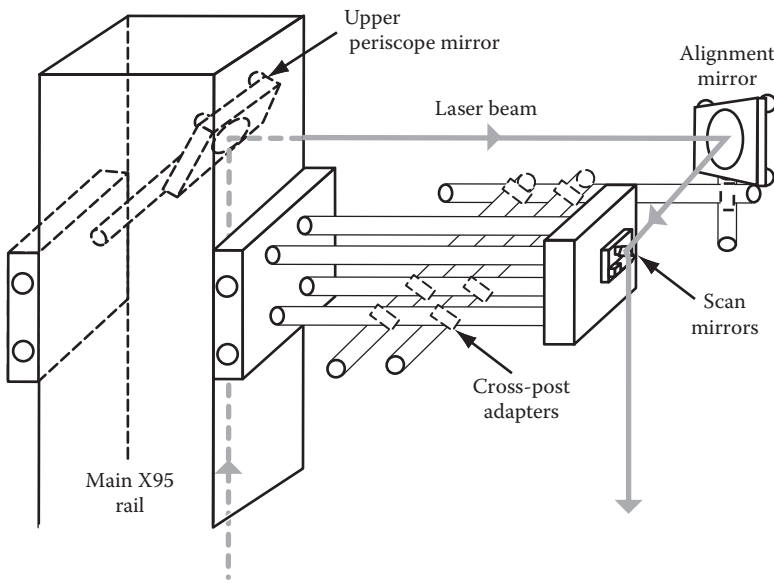
FIGURE 3.18 The uppermost attachments to the X-95 rail that form the microscope. The attachment at the rear holds the top periscope mirror. The attachment at the front holds the rod assembly, constructed of stainless steel posts, right angle cross-post adapters, and a X-95 carriage, that connects to the scan mirrors and the alignment mirror.

directly mounted to the custom-designed headstage adapter, reinforced with diagonal cross-bracing, that is in turn mounted on a X-95 carriage.

Focusing stage. Axial alignment of the objective is achieved with a commercial modular focusing unit (Nikon) (Figure 3.19). This unit allows 30 mm of vertical motion, which facilitates changing preparations and objectives. A custom-made adapter plate is attached to the focusing unit, and the objective holder is mounted to the adapter plate. The objective holder consists of a custom-made groove plate and five Microbench™ (Linos Photonics) parts in the configuration shown in Figure 3.19.

It is often desirable to step along the focus axis either as a means to automate the choice of focal plane or to systematically acquire a set of successive images. The modular focus unit is easily coupled to a stepping motor by capturing the fine focus knob in a friction-held cap. For the case of relatively fast movements along the focus axis, one can use long-range piezo-drivers such as the no. P-725 from Physik Instrumente, Karlsruhe/Palmbach, Germany.

3.4.5 PATH ALONG MICROSCOPE: PLASMA-MEDIATED ABLATION

The amplified laser beam used for ablation is either derived from the same oscillator that is used to image or from a different Ti:Sapphire oscillator, each of which will operate at a center wavelength near 800 nm. We thus combine the imaging and ablation beams with a polarizing beamsplitter that is located directly below the
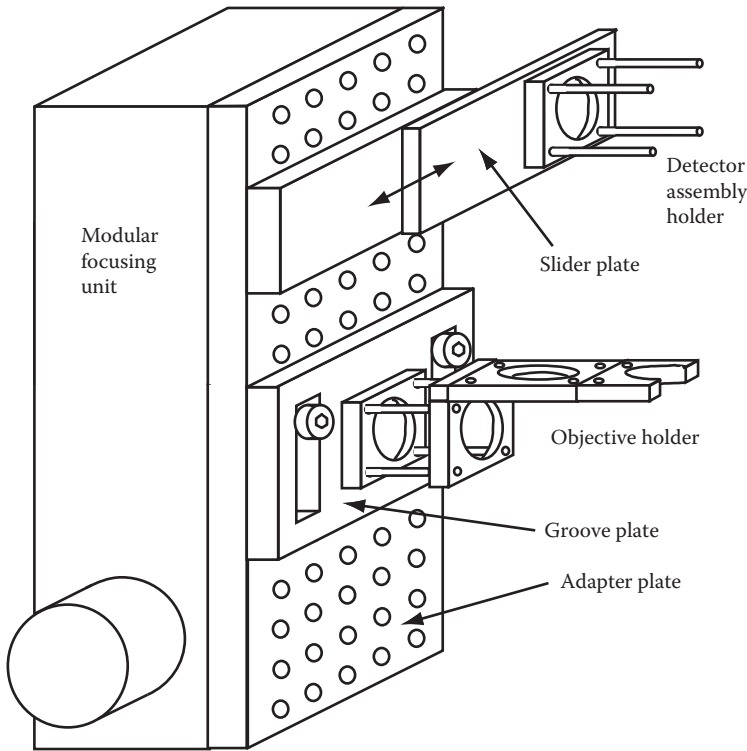
FIGURE 3.19 The focusing unit that supports the objective and detector assembly on the main X-95 rail. The objective holder consists of Microbench™ parts (Linos Photonics) connected to a Modular Focusing Unit (Nikon) by two custom-made plates; an adapter plate with 20 quarter-inch holes spaced on 1″ centers that is driven by the Modular Focusing Unit, and a groove plate that supports the objective holder. The detector assembly holder consist of a slider plate and Microbench™ parts, and is mounted on the adapter plate.

tube lens (Figures 3.16 and 3.17). We use a 25-mm^2 beamsplitter that is glued to a mount along the back edge. The divergence of the amplified beam must be adjusted to ensure that both the focus of the imaging beam and that of the ablation beam lie in the same plane.

3.4.6 Path along Microscope: Detection

3.4.6.1 Detector Assembly

The detector assembly is attached to the focusing unit via the adapter plate. The entire detector assembly is placed on a slider plate so that the dichroic beamsplitter can be removed from the visual path, and then replaced without changing its alignment relative to the other collection optics. The back panel of a slider plate is mounted to the adapter plate, and a Microbench™ mounting plate is attached to the front panel of the slider plate. Four rods inserted into the mounting plate are used to attach the detector assembly by its rear left face.

The detector assembly is constructed mainly with Microbench™ parts in a double-cube configuration (Figure 3.20A). Nine square plates are formed into a rectangle using four long rails and two short rails. Two f_{CL} = +27 mm lenses serve as the collectors and are loaded into the far right plate and the right rear plate. Eight 2″ rods are inserted into the same plates to provide a mounting area for the glass filters and detectors. Infrared blocking filters and appropriate band-pass filters are mounted in additional square plates that slide directly onto the rods. The compact PMT detectors are mounted in a customized holder (Figure 3.20B) that also slides directly onto the rods. This assembly can be readily extended to three detectors.

The two dichroic beamsplitter mirrors, one of which separates the incident laser light from the emitted fluorescent light (beamsplitter #1) and one of which resolves the fluorescent light into separate spectral bands (beamsplitter #2), are held on prism mounts that are inserted through the front left plate and bottom right plate. The laser enters through the top left plate and exits through the bottom left plate of the double
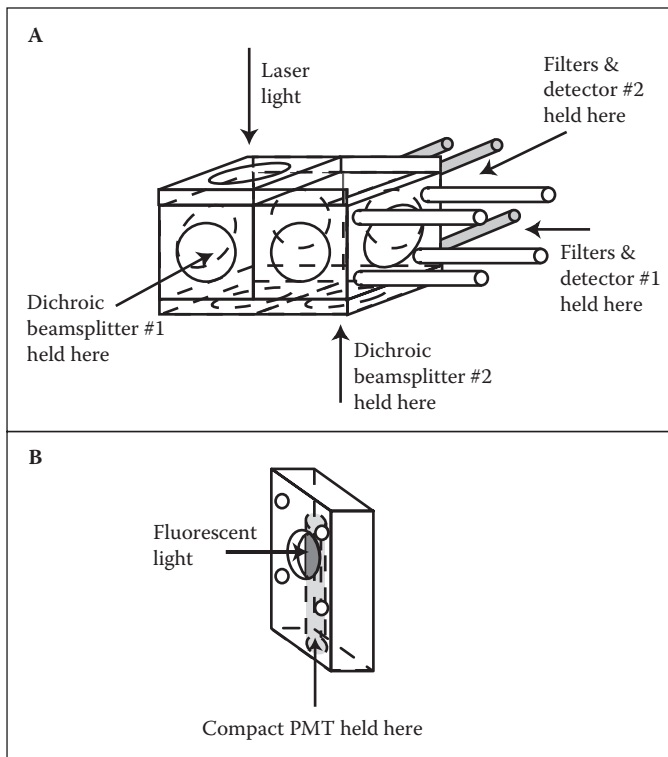
FIGURE 3.20 Illustration of the detector assembly. (A) The main assembly is fabricated from Microbench™ parts. Dichroic beamsplitters are mounted on adjustable prism mounts and placed in the labeled openings. Filter blocks and the compact photomultiplier tubes (PMTs) are held by the four rods protruding along each path. (B) The PMT case is a custom-made aluminum cage that is designed to be compatible with Microbench™ parts and the compact Hamamatsu PMTs.

cube. The edges between the plates are sealed to be light-tight with black silicone sealant (RTV 103; GE); this sealant is easily removed from anodized surfaces. Lastly, small black-anodized sleeves are inserted as baffles between the square plates that hold optics and filters to prevent stray light from entering the detector assembly.

3.4.6.2 Collection Filters and Optics

The first element in the collection pathway (Figure 3.21) is the long pass dichroic beamsplitter mirror, that is, $\lambda_{cut} = 700$ nm (no. 700DCXRU; Figure 3.22), that transmits light at the laser excitation wavelength while deflecting fluorescent light toward the detectors. This is followed by the first of two high-efficiency laser-blocking filters (E680SP-2P; Figure 3.22) to reduce the background level and associated noise that is caused by scattered incident laser light. A second dichroic is used, if necessary, to separate the fluorescent signals from two different fluorescent indicators. For example, we use a $\lambda_{cut} = 505$ nm DRLP to resolve light from yellow fluorescent protein (YFP) versus cyan fluorescent protein (CFP). The signal in either path is then imaged onto the active area of a PMT by a short focal length lens. A second laser-blocking filter (E680SP-2P) is placed in front of the detector to further reduce the background level (Figure 3.21). An alternate solution is to use 2 mm of Corning no. BG39 glass. Finally, additional interference filters, that is, $\lambda_{pass} = 525 \pm 5$ nm to isolate YFP and $\lambda_{pass} = 485 \pm 11$ nm to isolate CFP, are placed in the detection pathway as needed.

In the collection assembly, a $f_{CL} = +27$ mm lens of $D_{CL} = 30$ mm diameter is placed at $l_1 = 120$ mm from the back aperture of the objective and at $l_2 = 35$ mm from the detector (Figure 3.21). In this configuration, the back aperture is imaged onto the detector surface with a magnification of 0.29 times. Therefore, a $D_{BA} = 7$ mm back aperture is imaged to a 2.0 mm circle at the PMT active surface.
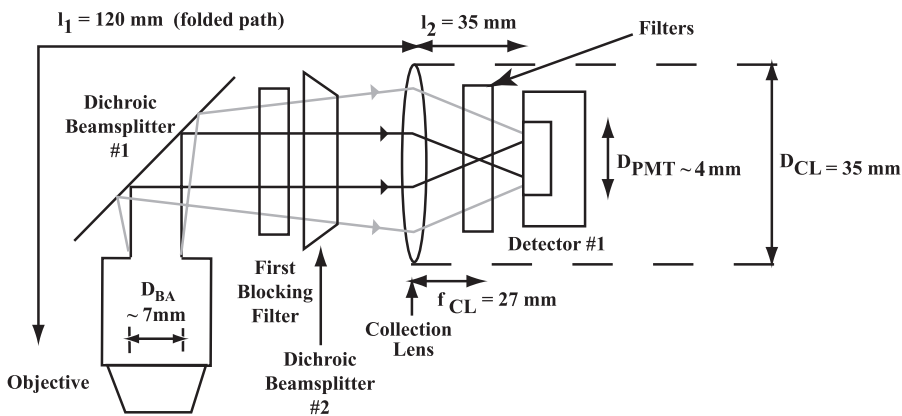

FIGURE 3.21 Detailed schematic of the detector assembly. The positions of both dichroic beamsplitters are shown; however, for clarity, we omit the optics and detector for the second, otherwise equivalent, pathway. Unscattered fluorescent light is depicted as dark lines, while scattered fluorescent light is depicted as gray lines.
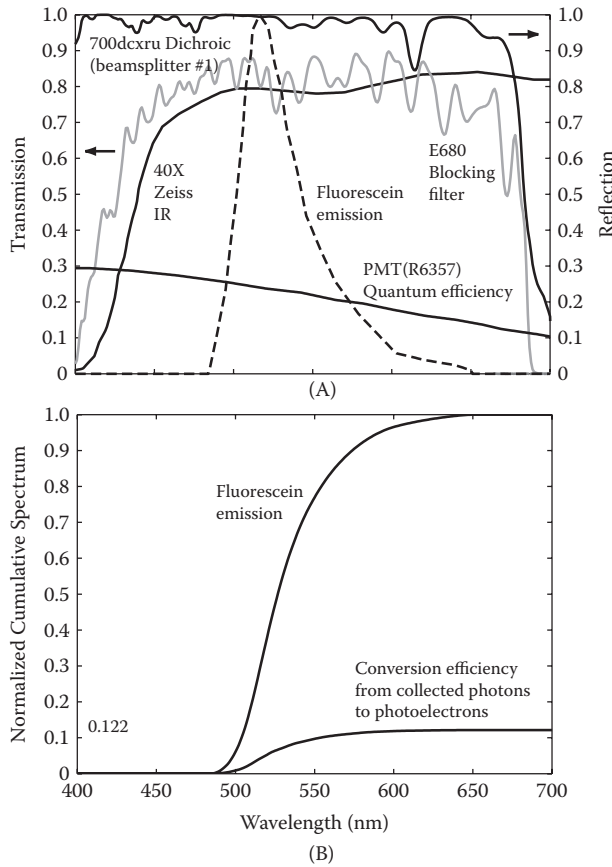
FIGURE 3.22 Throughput of the detector system for the conversion of detected photons into photo electrons. (A) Spectrum for fluorescein, along with the reflection spectrum of the dichotic filter that acts as beamsplitter #1 (Figure 3.21), the transmission spectrum of the blocking filter, the throughput of the objective, and the quantum efficiency of the photodetector. (B) Conversion efficiency (Equation 3.29), calculated as the cumulative, with two blocking filters in place.

3.4.6.3 Photodetectors

The detectors in our system are a mixture of Hamamatsu R6357 photomultiplier tubes and H7422-40 PMT modules with a cooler and modified for higher current. We chose these PMTs because of their spectral properties, high sensitivity, and relatively small size. The R6357 is powered by a external high-voltage supply, has an active area that accepts a 4-mm-diameter spot, a quantum efficiency of 0.30 at $\lambda = 550$ nm, and a maximum output current of 10 μA. This tube can be used for high photocurrents, that is, $n_{pulse}^{photoelectrons} \geq 1$ (see Section 3.3.7.1). In contrast, the H7422-40 is powered by

an internal supply, has an active area that accepts a 5-mm-diameter spot, a quantum efficiency of 0.40 at $\lambda = 550$ nm, and a maximum output current of 2 µA. This tube saturates for high anode currents, and the H7422-40 MOD with a 50 µA shut-down circuit, 25-times higher than the unmodified tube, is recommended.. Independent of the detector, the output from the PMT is a pulse of current whose width is 1 to 2 ns.

3.4.6.4   Detection Electronics

The scheme to detect the emitted photons depends on the number of photoelec-trons/pulse that are generated at the detector. When the number of photoelectrons/pulse is near 1, or greater, the total current is measured. When the number of photoelectrons/pulse is much less than one, photon-counting is advantageous as it eliminates extra variability from differences in the amplitude of the amplified photoelectrons, that is, pulse-height variability, as well as some thermal contributions to the noise.

We previously estimated the number of emitted photons (Section 3.3.7.1). The number of photoelectrons is found by multiplying the number of collected photon by the integrated throughput of all of the filters and the photocathode. For this analysis, we note the additional definitions:

$n_{pulse}^{photoelectrons} \equiv$ Number of electrons produced at PMT photocathode per pulse

$QE(\lambda) \equiv$ Quantum efficiency of photocathode

$O(\lambda) \equiv$ Transmission of objective

$R_{D1}(\lambda) \equiv$ Reflection coefficient of beamsplitter #1

$T_k(\lambda) \equiv$ Transmission coefficient of k-th filters (or beamsplitter)

$F_{dye}(\lambda) \equiv$ Fluorescent emission spectrum of dye

Then

$$n_{pulse}^{photoelectrons} = n_{conversion}\ n_{pulse}^{collect} \tag{3.28}$$

where

$$n_{conversion} = \frac{\displaystyle\int_0^\infty d\lambda\ R_{D1}(\lambda)\ T_1(\lambda)\cdots T_k(\lambda)\ O(\lambda)\ QE(\lambda)\ F_{dye}(\lambda)}{\displaystyle\int_0^\infty d\lambda F_{dye}(\lambda)} \tag{3.29}$$

The choice of a R6357 PMT and the filters discussed above (Section 3.4.6.2) leads to a conversion of 0.12 photoelectrons per photon collected by the objective (Figure 3.22) for fluorescein dye; this number should change little with filters optimized for a given

dye. Note that additional losses will occur from vignetting and reflections by the detection beam optics.

For the case of neurons labeled with Calcium Green, we estimated $n_{pulse}^{collect} \approx 3$ photons/pulse (Section 3.3.7.1), which leads to

$$n_{pulse}^{photoelectrons} \approx 0.3 \text{ photoelectrons/pulse.}$$

The probability of two or more photons arriving at the detector on a given pulse is small but non-negligable, i.e., 4%. This photocurrent may be effectively measured with either analog electronics, which is a necessity for $n_{pulse}^{photoelectrons} \sim 1$ or more, or digital electronics, which is far best for $n_{pulse}^{photoelectrons} \ll 1$.

With regard to analog detection, the expected anode current from a R6357 PMT, with a gain of 4×10^6, is 15 μA for $n_{pulse}^{photoelectrons} \approx 0.3$; this current can be up to 2-times less as a result of spatiotemporal aberrations caused by the dipping objective (Section 2.5.2). While this current exceeds the 10 μA stated maximum anode current, the average current in a scanning system is well within bounds. The output current of the PMT is converted to a voltage through a 10 kΩ resistor, followed an impedance buffer with a gain of 10 and a 50 Ω line driver (no. OPA637 operational amplifier followed by no. OPA633 unity gain buffer; Burr Brown, Tuscon, Arizona), for a measured time-constant of $\tau = 0.4$ μs. This is followed by either an adjustable low-pass filter (D01L8L, Frequency Devices, Ottawa, Illinois) or an integrator of local design.

Signals from weak fluorescence, such as the intrinsic in vivo levels of the flavin molecules, whose cross section is two-orders of magnitude less than that of fluorescein, or from low expression levels of green fluorescent protein (GFP) and its derivatives, are best recorded by photon counting. Here, the output of the PMT is converted to a voltage through a 50 Ω resistor, amplified by a broadband voltage-to-voltage converter, then compared with a threshold value to estimate if a photo-current pulse has occurred. The threshold operation removes noise caused by pulse-height uncertainty, and this improves the signal-to-noise ratio by a factor of $\sqrt{(1 - g^{-M})/1 - g^{-1}}$,[60] where g is the gain per stage and M is the number of stages of the PMT. Typically, $g = 5$ and $M = 9$, so that the increase is about 12%. Additional improvement comes from rejection of thermionic current pulses from the dynodes. A photon-counting system for TPLSM that can acquire continuously is under testing at the time of this write-up (Driscoll, Nguyen, White, Tsai, Squier, Cauwenberghs, and Kleinfeld, unpublished).

3.4.6.5   Scan Mirrors and Drivers

We use state-of-the-art galvanometer optical scanners from Cambridge Technology, Inc. These scanners are capable of rotations up to ± 20° and rates of up to 3 kHz at reduced deflection angles. We typically use angles of ± 5° or less; for a 40-times magnification, deflections of ± 1° correspond to distances of ± 40 μm in the focal plane. The scanners are designed to hold $D_{SM} = 3$ mm aperture mirrors that are provided by the manufacturer.

3.4.7   Scan and Acquisition Electronics

The scanners and associated electronics and computer boards must be chosen and configured to provide horizontal and vertical scans that are synchronized to each
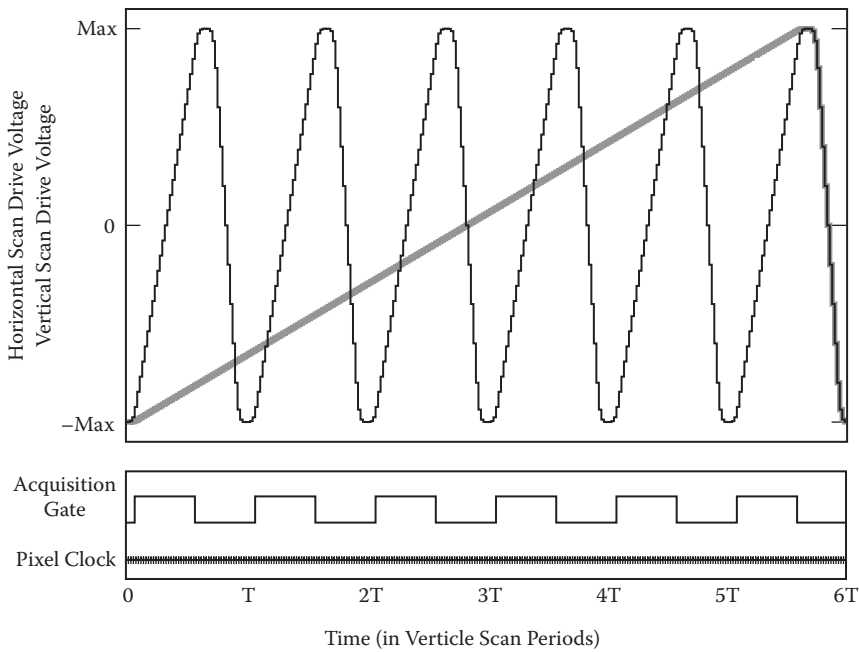
FIGURE 3.23 Cartoon illustration of the drive signals for the scan mirrors and data acquisition for a standard rater pattern. All functions are synchronized to the continuously running pixel clock. The data acquisition gate is active for a portion of the fast scan. During this time window, data is acquired at the pixel clock rate. The fast scan signal is updated which each pixel clock tick, while the slow scan signal is updated once per fast scan cycle.

other, so that they define a raster, as well as synchronized to the data acquisition. This is illustrated for a standard raster in Figure 3.23. We use the model PCI-6110 from National Instruments (Austin, Texas), which has two 16-bit digital-to-analog (DAC) channels and four analog-to-digital (ADC) channels that acquire as rapidly as 0.2 µs/sample; DACs support the horizontal and vertical scans. An additional DAC board, such as the model PCI-6711 from National Instruments, is used to control the piezoelectric *z*-focus and intensity controls. Lastly, for the case of photon counting where high-speed digital input from an external counter is necessary, we use model PCI-6534 from National Instruments, which acquires 32 bits of parallel input as rapidly as 0.05 µs/sample. All interface boards communicate with each other via the Real-Time System Integration (RTSI) bus; a 34-pin cable connects all of the RTSI connectors to form the bus.

3.4.8 SOFTWARE

Software to control TPLSM has been described and, for the large part, can be adapted to different systems independent of the particulars of the hardware.[61–64] Our current system, MPScope,[62] is further described in an accompanying article and is fully integrated with the X-Y stage motors for serial ablation across regions.

3.5 PERFORMANCE AND APPLICATIONS

3.5.1 System Validation

After our system was constructed and tested, various calibrations were performed to determine the exact values of scale factors, true lateral resolution, axial resolution, and uniformity of the image.

3.5.1.1 Spatial Scales

The horizontal and vertical scale factors are determined by imaging a circular opening of known diameter—typically, a 50-µm metal pinhole that is illuminated with a 800-nm light. No fluorescent dye is used; the reflected light from the polished surface is sufficiently strong so that enough 800-nm light leaks through the dichroic beamsplitter and blocking filters to provide a signal. The diameter along both the horizontal and vertical axes, as measured in pixels, yields the scale factor at a particular zoom setting. As the image is best viewed without distortion, the gain for the horizontal and vertical directions should be identical. This calibration is repeated at several magnifications to ensure the linearity of the scale factor as a function of magnification.

3.5.1.2 Resolution

The resolving power of the microscope can be determined by imaging fluorescent beads whose diameter is below the optical resolution limit. The beads must be dilute, so that an individual bead can be identified, and they should be suspended in agarose to reduce motion during imaging. Figure 3.24 contains an image of 0.2-µm yellow-green fluorescent microspheres (Polysciences, Inc., Pennsylvania), suspended in 2% agarose, that was obtained with our microscope using a 40-times magnification water immersion objective (Zeiss). The full-width at half-maximal intensity from individual beads in the lateral dimension was calculated from the acquired images (Matlab™; Mathworks, Massachusetts). The axial resolution is obtained by compiling a series of images taken at different axial positions and calculating the intensity profile of a single bead as a function of axial position. We determined that the spatial resolution (FWHM) for our system was

$$d_{\text{lateral}} \cong 0.5 \text{ µm and } d_{\text{axial}} \cong 2 \text{ µm}.$$

The value for d_{lateral} is consistent with $2\omega_0 = 0.5$ µm, while that for d_{axial} is significantly larger than $2z_{\text{confocal}} \cong 0.7$ µm but consistent the axial resolution for planar illumination.[27]

3.5.1.3 Ablation Threshold

To establish the relation between the energy of the pulses and the spatial extent of point ablations, we systematically varied both the energy per pulse and the number of pulses to generate an array of ablation sites in fixed neocortex from rat. The ablations took the form of small craters of graded sizes with the largest holes made by 510 consecutively
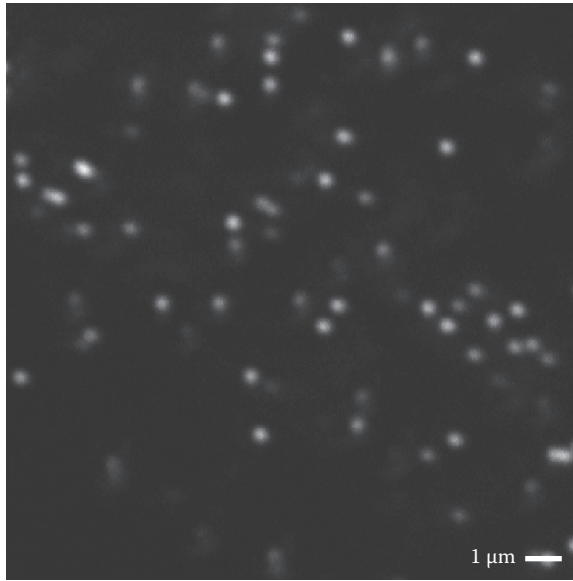
FIGURE 3.24   Image of fluorescent microspheres that are used to establish the resolution of our two-photon laser scanning microscope. The microspheres are 0.2 µm latex balls (no. 17151; Polysciences, Inc., Warrington, Pennsylvania) that are coated with fluorescein.

delivered 5 µJ pulses (Figure 3.25A). The bright border surrounding each hole stems from an increase in autofluorescence that accompanies the laser cutting.

We observed the formation of a crater at a minimum energy of 0.63 µJ for a single pulse application with this array (Figure 3.25B), which corresponds to a fluence of $F_\mathrm{T} \approx 3$ J/cm^2 for the parameters of our beam. This is in agreement with the value of the threshold for ablation of bovine brain tissue that was freshly dissected[65] as well as ablation of various glasses.[66] The ablation volume has a greater depth along the z axis than width along the X and Y axes (Figure 3.25B), consistent with a simple model (Equation 3.9). Further, an increased number of laser pulses only weakly compensates for lower pulse energies, that is, by approximately twofold for 130 pulses Figure 3.25A). Thus, ablation is most efficient, in terms of total energy expenditure, with one or few pulses whose fluence lies above the threshold value.

3.5.1.4   Spatial Uniformity

The homogeneity of the scan was determined by imaging a spatially uniform field of fluorescence (i.e., a Petri dish filled with a 100 µM solution of fluorescein). This method finds inhomogeneities in the detection pathway as well as the in the scan pathway. The profile obtained in this manner, shown in Figure 3.25, is observed to be stable for a given configuration of the microscope, albeit slightly anisotropic (Figure 3.11). The measured profile can be used as a calibrated filter for images taken with this system; postprocessing with this filter yields a fluorescent image that is free of spatial intensity distortions.
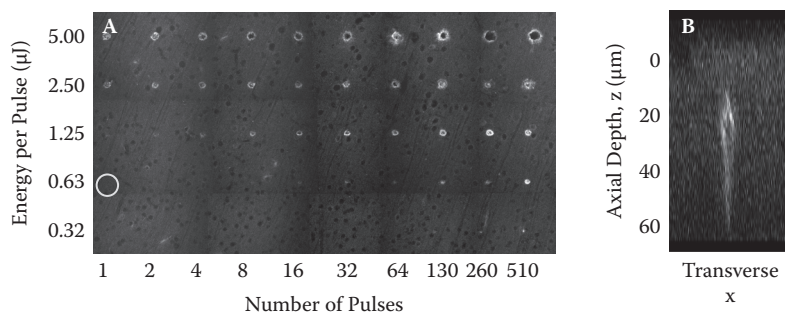
FIGURE 3.25 Threshold for plasma-mediated ablation in fixed neocortex. (A) Array of ablation craters, in fixed neocortical tissue from rat, as a function of the energy per pulse (vertical axis) and number of laser pulses (horizontal axis). Ablation was performed with a 10-times magnification, 0.2 NA air objective. The distance between craters is 100 μm. The image is a single section obtained with TPLSM at $\lambda = 760$ nm to highlight intrinsic fluorescence. The yellow circle highlights the lowest energy at this NA for clearly observed ablation in a single pulse. (B) Transverse maximal projection through the ablation volume created by a single pulse at an energy of 0.63 μJ per pulse. Note the intrinsic fluorescence that surrounds the ablated dark, inner region.

3.5.2 Pulse Width

The shape and duration of the incident laser pulse critically affects the efficiency of nonlinear optical processes (Figure 3.3). The ultrashort pulses used for multiphoton microscopy are typically one hundred to a few hundred femtoseconds in duration. Since no electronic photodetector has the necessary time resolution to measure such time-scales, optical pulse measurement techniques must be used. An autocorrelation measurement is an effective and relatively simple method of monitoring the pulse length and is simple to implement.

3.5.2.1 Autocorrelation

In an autocorrelation measurement, a laser pulse is split into two identical copies. One pulse is delayed relative to the other by a time, τ, which results in two pulses with electric fields $E(t)$ and $E(t + \tau)$. The two pulses are recombined and used to excite a nonlinear process such as two-photon fluorescence. The interferometric autocorrelation function, denoted $I_{AC}(\tau)$, is given by the sum of $E(t)$ and $E(t + \tau)$, raised to the fourth power, and averaged over time. This appears as an oscillatory signal with an envelope that depends on the delay time τ (Appendix B). A convenient feature of this autocorrelation is an 8:1 ratio of the amplitude of the maximum from zero to the amplitude of the constant background that is produced by widely separated pulses. Achieving this ratio indicates that the apparatus is well aligned. In the case that the laser pulse has essentially no chirp, the FWHM of the autocorrelation is equal to $\sqrt{2/ln2}$ times (1.7 times) the FWHM of the intensity of the original pulse.

Our laser system and microscope was set up without external pulse compression. We constructed an autocorrelator[67,68] that could be switched into the beam path (Figure 3.15). We found that although the commercially purchased Ti:Sapphire laser should output pulses around 120 fs, the pulses at the microscope objective are typically closer to τ_{FWHM} = 250 fs, as shown by a fit of a model autocorrelation (Appendix B) to the measured autocorrelation function (Figure 3.27A). This pulse is weakly chirped (1% or ~8 nm), as evidenced by the curvature in the wings of the autocorrelation function (∗ in Figure 3.27A). The increase in pulse width represents the cumulative effect of optics throughout the entire TPLSM system (Figure 3.15). Note that, by judicious tuning of the laser, we could achieve pulses with minimal chirp and with widths of τ_{FWHM} = 180 fs (Figure 3.27B and Equation 3.A.5).
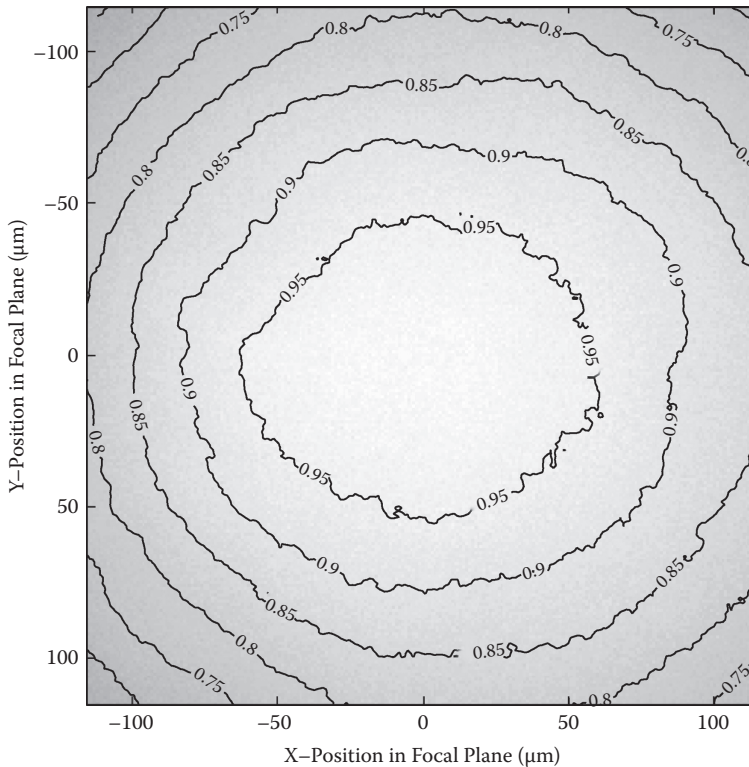

FIGURE 3.26 Contour plot of spatial uniformity of the two-photon generated and detected fluorescence measured with a 40-times magnification lens. Note that the decrement across the entire field exceeds that calculated for the generation of the fluorescence alone (Figure 3.11), but that the decrement across the central 100 μm of the field is less than 10%.
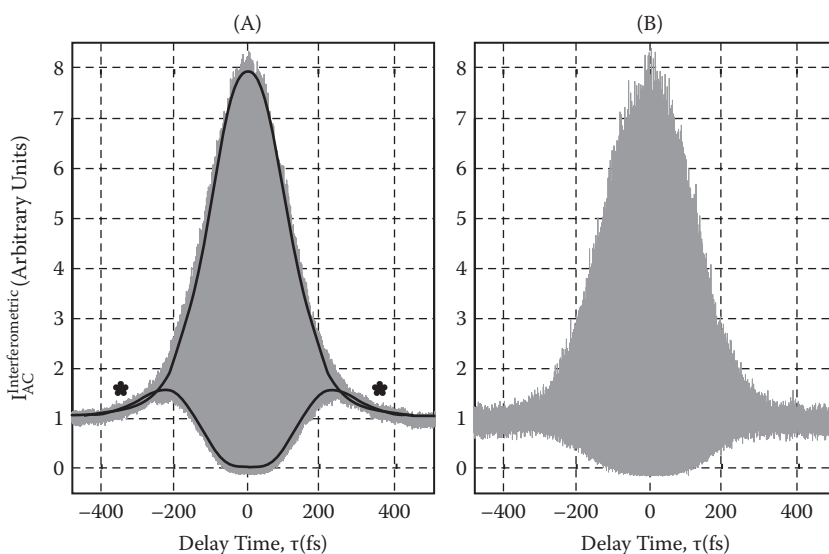
FIGURE 3.27 The interferometric autocorrelation function (Equation 3.A.4) measured for laser pulses measured at the position of the objective with our two-photon laser scanning microscope. (A) The autocorrelation under typical levels of performance. The asterisks indicate additional curvature as a result of chirp in the pulse. The envelope of the autocorrelation is fit with the calculated autocorrelation for a chirped pulse (thick envelope), from which we estimate a FWHM of the laser pulse to be 250 fs. The chirp parameter is $b = 5 \times 10^{-5}$ fs^{-2}; this corresponds to a factional shift in frequency of $2 \bullet b \bullet \tau_{FWHM} \bullet \omega = 2 \bullet b \bullet \tau_{FWHM} \bullet \lambda_0 / 2 \bullet \pi \bullet c = 0.01$, where $\lambda_0 = 800$ nm and c is the speed of light. (B) The autocorrelation for a pulse with essentially no chirp, that is, $b = 0$. For this case we estimate a FWHM of the laser pulse to be 180 fs (Equation 3.A.5).

3.5.2.2 Comparison of Objectives

To compare the performance of various brands and types of objectives, each with different glasses and detailed construction, identical laser parameters were measured using a number of objectives on the microscope. We found that the variations of the measured pulse width from the objectives were not significant at a given wavelength nor was there a significant change in pulse-width over the 780 to 880 nm range of wavelengths for the incident light (Figure 3.28).

3.5.2.3 Effect of the Scan and Tube Lenses

One concern in the construction of the microscope is dispersion by the tube and scan lenses. With the standard tube lens in the trinocular and an achromat as the scan lens, the pulse width was $\tau_{FWHM} = 230$ fs as compared with $\tau_{FWHM} = 180$ fs with only the objective in the microscope pathway.

3.5.3 Alignment of the Imaging and Ablation Foci

To achieve co-planar ablation at the center of the imaging field, the ablation and imaging beams must be collimated and co-linear when they enter the back aperture
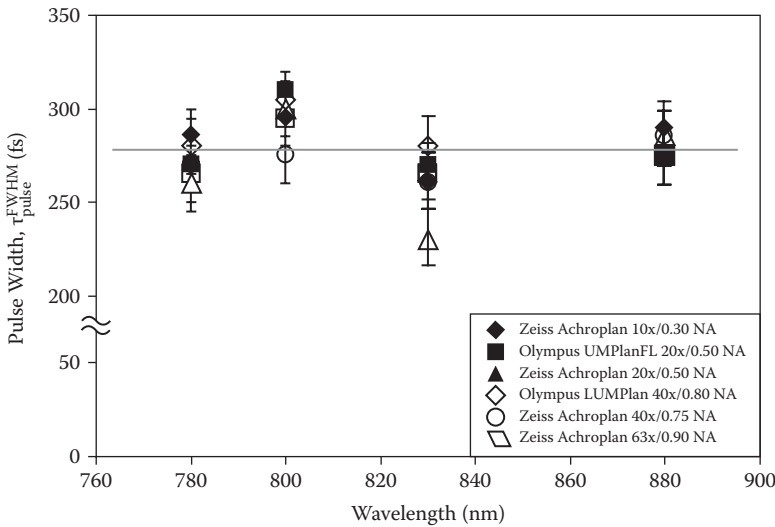
FIGURE 3.28 Plot of the FWHM of the laser pulse width measured for six different common objectives as a function of excitation wavelength. There is no significant difference in pulse width between lenses.

of the objective. This is achieved by temporarily replacing the objective with a mirror mounted at 45°, which diverts the beam to a distant target screen. The imaging beam scanners must be powered and set to a minimal scan for this alignment. Collimation of each beam is verified individually by comparing the beam profile near the 45° mirror and at the target screen. Co-linearity is achieved by overlapping the two beams at both locations. Adjustments to beam collimation are achieved by manipulation of the appropriate beam telescope (Section 3.4.3). Adjustment of co-linearity is achieved by adjustment to the two mirrors in the ablation beam path directly upstream of the polarizing beamsplitter.

The required precision of alignment can be calculated in a geometric optics limit by replacing the objective with a simple positive lens. For example, we can replace a 40-times magnification objective with a 4-mm focal length lens and calculate the beam divergence as:

$$\Delta f = f_{obj} - \left(\frac{1}{f_{obj}} - \frac{1}{f_{beam}} \right)^{-1} \tag{3.30}$$

where Δf is the axial focus shift in the sample, f_{obj} is the equivalent focal length of the objective, and f_{beam} is a measure of the beam divergence that is equal to the distance between the tube lens and the focus of the ablation beam. Thus, an ablation beam divergence corresponding to an 8-m focus will manifest as a 12% change in beam diameter at a target placed 1 m away, and result in an axial focal shift of 4 μm in the sample. The lateral deviation from co-linearity is given by:

$$\Delta r \simeq - f_{obj} \ \theta_{input}^{radians} \tag{3.31}$$

where Δr is the lateral deviation of the ablation focus from the center of the imaging field, and $\theta_{input}^{radians}$ is the deviation angle of the ablation beam from co-linearity with the imaging beam. Thus, a 1° deviation will manifest as a 17-mm offset of the two beams at a target located 1 m away and result in an ablation spot in the sample that is 70 μm from the center of the imaging field.

Experimental verification of beam alignment can be achieved by imaging and ablating the interface of a glass slide immersed in a fluorescent solution, such as aqueous fluorescein. The glass surface will appear in dark contrast to the fluorescent solution, while ablation craters formed at the interface will fill with solution and appear fluorescent.

3.5.4 EXAMPLE APPLICATIONS

3.5.4.1 In Vivo Cortical Blood Flow

A unique aspect of TPLSM is the ability to observe anatomical and functional signals in the brains of living animals deep to their pial surface.[4] As an example that used the microscope described above, we consider the flow of red blood cells (RBCs) in individual capillaries in rat cerebral cortex[3] (Figure 3.29). A cranial window is prepared over whisker barrel sensory cortex, and the dura is removed; a metal frame and closed surgical window are attached to the skull for stable mounting of the preparation to the microscope table.[41] The blood stream is labeled with fluorescein-conjugated-dextran (2 MDa). A single optical section obtained 100 μm below the pial surface is shown in Figure 3.29A, and the maximal projection reconstructed from 41 individual planar images, ranging in depth from 80 to 120 μm below the pial surface of the brain, is shown in Figure 3.29B. Notice that individual RBCs appear in the capillaries as dark stripes that correspond to locations where the fluorescent dye was excluded from the lumen of the vessel during the scan.

Line scans may be taken repeatedly along an individual capillary to produce a continuous measure of blood flow. The spatial coordinate is taken to be along the direction of the scan, while the perpendicular direction represents the temporal coordinate. As the RBC moves along the capillary, its position along the line scan changes from scan-to-scan, thereby tracing out a dark line, as shown for three examples (Figures 3.29C–E). The data of Figure 3.29C shows continuous flow, and the analysis of this data provides information regarding three parameters of capillary blood flow: blood cell speed, blood cell flux, and blood cell linear density, where flux = linear density × speed. The slope of the line is the inverse of the instantaneous speed, that is, speed = $|dt/dx|^{-1}$. The spacing between the lines along the temporal coordinate direction is a measure of the cell flux, while the spacing between the lines along the spatial coordinate direction is a measure of the cell density. The line scan data of Figure 3.29D contains a short vertical region, indicative of a momentary stall of the RBCs, while that of Figure 3.29E illustrates some of the high variability in flow that may be observed.
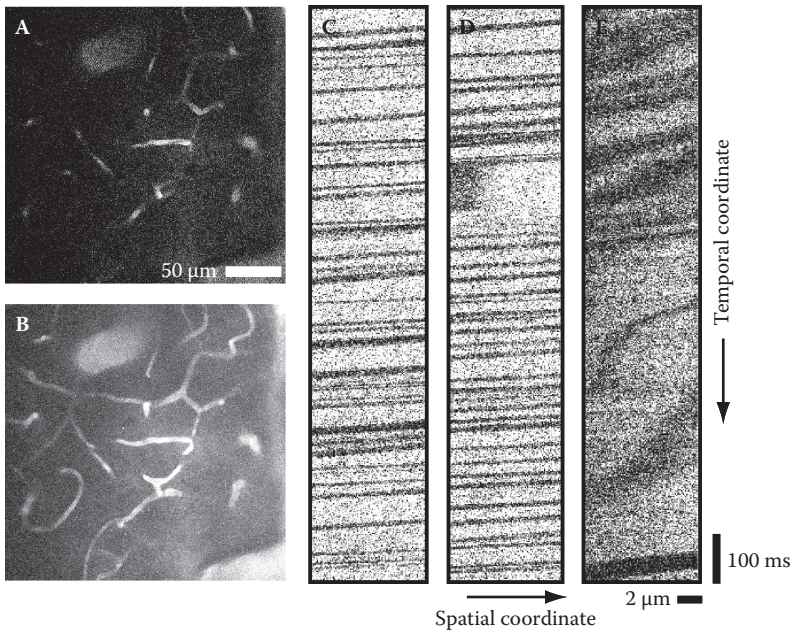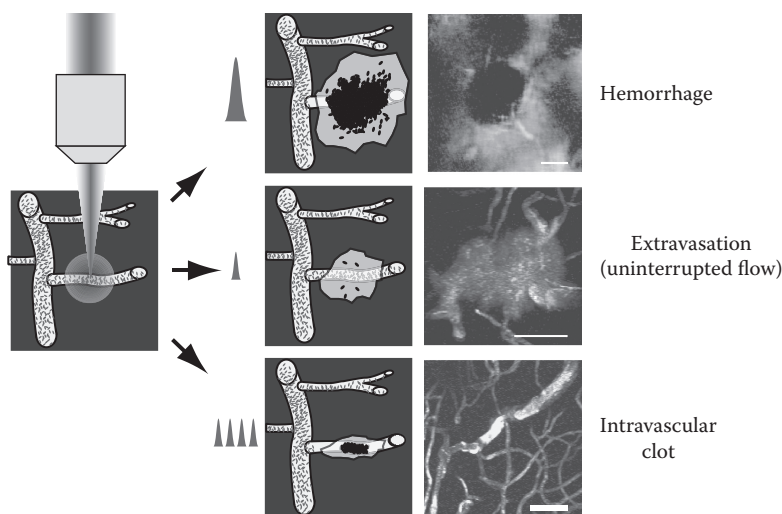
FIGURE 3.29   In vivo TPLSM used to image the capillary bed in rat vibrissa primary sensory cortex. An optical window was prepared over this region and the bloodstream was labeled with 2MDa fluorescein conjugated-dextran. (A) An single planar image from a depth of 100 μm below the pial surface of cortex. Notice that individual RBCs, which occlude fluorescent dye, appear in the capillaries as dark stripes. (B) A maximal projection reconstructed from 41 planar images, as in part A, taken between 80 and 120 μm below the pia. (C–E) Line scan data taken along single capillaries. Panel (C) shoes relatively fast, uniform flow. The thickness of the dark line may reflect the orientation of the red blood cell. Panel (D) shows flow that is interrupted by a brief stall while panel (E) shoes flow that is highly irregular.
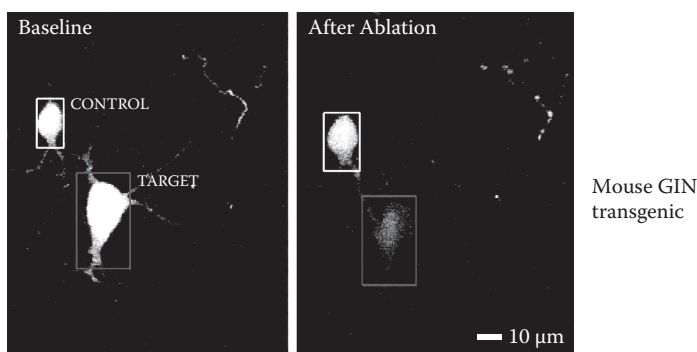
3.5.4.2   Perturbation of Vasculature and Neuronal Processes

The integration of photo-induced plasma-mediated ablation, through the use of high-energy laser pulses, combined with imaging of fluorescently labeled tissue, through the use of TPLSM with low-energy pulses, allows the targeting and real-time monitoring of photodisruption of biological microstructures. We show examples for the cases of individual labeled blood vessels and individual labeled neuronal somata.

We first consider the use of plasma-mediated ablation to perturb the flow of blood in targeted subsurface microvessels in cortex without affecting the area surrounding the vessel.[13,69] Rodents were prepared as described above. The region of interest was imaged with TPLSM using 40-times magnification dipping objective, and then a vessel was selected for targeting with the amplified laser source. Vessel rupture and hemorrhages could always be attained at high laser energies (Figure 3.30a), typically 1 to 10 pulses at ~0.8 μJ/pulse. Disruption with low pulse energy, ~0.3 μJ/pulse, resulted in extravasation of the fluorescein dye in the blood plasma but uninterrupted

Hemorrhage

Extravasation
(uninterrupted flow)

Intravascular
clot

(A) Targeted subsurface microvascular disruption

Baseline

CONTROL

TARGET

After Ablation

Mouse GIN
transgenic

10 μm

(B) Targeted somatic ablation

FIGURE 3.30 (See color insert following XXX) In vivo TPLSM and plasma-mediated abla-
tion in rodent cortex. (A) Schematic and examples of three different vascular lesions that are
produced by varying the energy and number of laser ablation pulses. At high energies, photo-
disruption produces hemorrhages, in which the target vessel is ruptured, blood invades the brain
tissue, and a mass of RBCs form a hemorrhagic core. At low energies, the target vessel remains
intact, but transiently leaks blood plasma and red blood cells forming an extravasation. Multiple
pulses at low energy leads to thrombosis that can completely occlude the target vessel, form-
ing an intravascular clot. Scale bars, 50 μm. (B) Example of cell degeneration that is produced
by a single pulse to the center of a GFP-labeled interneuron. (From Migliori, Atallah, Tsai,
Scanziania, Kleinfeld, unpublished)

flow. Repeated pulses led to a clot that completely stopped RBC motion. Real-time
monitoring of the vasculature with TPLSM allows one to fully characterize the
actual insult and the functional response in the neighboring tissue.

We next consider the use of plasma-mediated ablation to destroy individual neu-
rons in hippocampal slice that are highlighted through the expression of GFP.[70]

Targeting of a single pulse to a labeled interneuron quenches the fluorescence in that cell without affecting that of a neighboring interneuron (Figure 3.30B). Similar studies have used plasma-mediated ablation to cut the axon of a neuron rather than damage to soma of the neuron.[12,71]

APPENDIX A: PARTS AND VENDORS FOR THE TPLSM

MECHANICAL

The $8' \times 4' \times 1'$ antivibration air table was purchased from Newport (Irvine, California). For mirror mounts, we used the Ultima® series from Newport and the Flipper Mounts from New Focus (Santa Clara, California). All mirror mounts were attached to standard 1/2″ posts and post holders from Newport that were held to the air table with clamping plates and forks from New Focus. Microbench™ parts were obtained from Linos Photonics (Milford, Massachusetts). The large X-95 rails and assorted clamps and brackets were purchased from a variety of vendors. The slider for the detector assembly was from New England Affiliated Technologies (SD Series; Lawrence, Massachusetts), and the Modular Focusing Unit was obtained from Nikon (part no. 883773; Garden City, New York). The motorized stages for X and Y translation of the preparation were obtained from Danaher Precision Systems (Salem, New Hampshire). Control for the stages was obtained with a model DMC4040 Motion Controller from Galil Motion Control (Rocklin, California). The power supplies for the controller were obtained from Acopian (Easton, Pennsylvania).

OPTICAL

All mirrors were $\lambda/10$ flatness, protected silver mirrors obtained from Newport. Water immersion objectives were purchased from Zeiss (Thornwood, NY) and Olympus. Dichroic beamsplitter #1 was a 700DCXRU (Chroma Technology; Rockingham VT); the beam blocking filters were E680-SP-2P from Chroma Technology (Rochester, NY), additional interference filters were from Omega Optical Inc. (Brattleboro, VT) and Chroma Technology (Rockingham). The wave plate, polarizing beamsplitter and intermediary optics were obtained from Newport and Linos Photonics. The scan lens is a Plan 1.0-times magnification dissection stereoscope objective with a focal length of 92.7 mm (Leica, Wetzlar, Germany).

SCANNERS

The scanning galvanometers and their drivers were obtained from Cambridge Technologies (Boston, Massachusetts). The scanners are Model 6210H Galvanometer Optical Scanners capable of ±20° maximum deflection. They have a 3-mm aperture and a 100-μs set time. We used their MicroMax™ 673XX Dual-Axis Servo Driver, which take a ±10-V analog input. The power supplies for the scan drivers were obtained from Acopian.

PHOTOMULTIPLIER TUBES

The model R6357 was specified for dark currents below 2 nA (Hamamatsu Corporation, Bridgewater, New Jersey) and powered by a model EW850-13 base (Hamamatsu Corporation) that is energized with a 0 to 2000 V DC adjustable power supply (Model PMT-20A/N; Bertan Associates, Hicksville, New York) configured to stay below the maximum rating of 1250 V that is required for this PMT. The model H7222 PMT module was specified with a modification for high threshold shut-off (Hamamatsu Corporation).

ELECTRONICS

The data acquisition board is a model PCI-6111E four channel analog input board from National Instruments (Austin, TX) that further contains two digital-to-analog converters that serve as the waveform generator for the scanning galvanometers. A model PCI-6710 Arbitrary Waveform Boards from National Instruments serves to control the Z-piezoelectric focus control. The stepping motor that controls the axial translation of the focus is a Vexta model PH268M-M1.5 (Herbach and Rademan Company, Moorestown, New Jersey). It has 400 steps per revolution, which results in 0.25 μm axial steps in combination with the Modular Focusing Unit.

LASER AND ANCILLARY EQUIPMENT

We have had good results with equipment from both Coherent, Inc. (Santa Clara, California), including a Verdi 10 W laser pumping a Mira 900F Ti:Sapphire oscillator, and Spectra Physics (a subsidiary of Newport, Inc.), including a Millennia 15 W laser pumping a Tsunami HP Ti:Sapphire oscillator. Additional equipment required for laser operation include:

1. Chillers, typically supplied with the lasers.
2. A dry nitrogen gas purge to facilitate laser operation for wavelengths longer than 900 nm.
3. An optical spectrometer to track the center frequency (e.g., USB2000+ [Ocean Optics, Inc., Dunedin, Florida])
4. An ~400-MHz bandwidth oscilloscope to aid in mode locking (e.g., Tektronix model TDS430A oscilloscope [Newark Electronics])
5. An infrared viewer (e.g., Find-R-Scope [FJW Optical Systems, Inc., Palatine, Illinois]) to aid in alignment of the microscope optics and major tuning of the oscillator.
6. A Si-based PIN diode photodiode to monitor the average laser power (e.g., Thor Labs [Newton, New Jersey] model DET10A). A calibrated energy meter (e.g., Newport model 818T-10, Newport) is used to calibrate the photodiode.
7. Safety glasses, to be worn when working near an unprotected beam line.

APPENDIX B: BASICS OF INTERFEROMETRIC AUTOCORRELATION

In the autocorrelation process, the laser pulse is split into two identical copies, and one is delayed relative to the other by a time τ. This results in two pulses with electric fields $E(t)$ and $E(t + \tau)$. These are subsequently multiplied together through a nonlinear process, such as two-photon excitation. For such a process, the instantaneous two-photon excited fluorescence for a given delay time is

$$I(t,\tau) = \left| \left[E(t) + E(t + \tau) \right]^2 \right|^2 .$$ (3.A.1)

The time resolution of the photodetector is much slower than the fluorescence duration, thus the output of the photodiode is the time average of $I(t, \tau)$ (Equation 3.A.1). This signal corresponds to the autocorrelation function, $I_{AC}(\tau)$, that is,

$$I_{AC}(\tau) = \int\limits_{-\infty}^{\infty} dt \left| \left[E(t) + E(t + \tau) \right]^2 \right|^2 .$$ (3.A.2)

To deduce the shape of the original pulses from the autocorrelation signal $I_{AC}(\tau)$, we assume a known original pulse shape. The autocorrelation signal can be calculated in terms of parameters describing the original pulse. The measured autocorrelation signal shape can then be used to deduce the original pulse parameters. Ultrashort laser pulses usually have Gaussian or secant-squared time envelopes. Since the Gaussian is a good estimate of the actual pulse shape and facilitates calculations, we assume a Gaussian profile for our beam. The electric field of the laser pulses can be described as

$$E(t) = E_0\, e^{-\frac{t^2}{a^2} + i2\pi\, v_0 t}$$ (3.A.3)

where the full-width-half-maximum (FWHM) of the intensity of the envelope of the pulse is $a\sqrt{2\ln 2}$, v_0 is the center frequency of the pulse, and the origin of time is arbitrary as $E(t)$ and $E(t + \tau)$ appear only in integrals over all of time (e.g., Equation 3.A.2).

The autocorrelation measurement can be set up in two ways. In an interferometric autocorrelation, fringes caused by the interference of the two pulses are observed. The two pulses are incident on the fluorescent material so that they are exactly colinear and are polarized in the same direction. In a noninterferometric autocorrelation, the fringes are smeared out either by introducing an angle between the beams or a difference in the polarization direction of the two pulses. While both autocorrelation methods give a measure of pulse length, the interferometric autocorrelation will also indicate the presence of chirp in the pulse.

The interferometric autocorrelation signal with $E(t)$ given by Equation 3.A3 is

$$I_{AC}^{\text{interferometric}}(\tau) \propto 1 + 2e^{-\frac{\tau^2}{a^2}} + 4e^{-\frac{3\tau^2}{4a^2}}\cos(2\pi\nu_0\tau) + e^{-\frac{\tau^2}{a^2}}\cos(4\pi\nu_0\tau). \quad (3.A.4)$$

The upper envelope and lower envelope can be found by setting $2\pi\nu_0\tau = \pi$ or 2π. A convenient feature of interferometric autocorrelation is the 8:1 ratio of the amplitude of the maximum from zero to the amplitude of the constant background. Achieving this ratio indicates that the apparatus is well aligned. In the case with unchirped pulses, the FWHM of $I_{AC}^{\text{interferometric}}(\tau)$ is related to the FWHM of the original pulse by

$$\tau_{\text{FWMH}} \approx \sqrt{\frac{ln2}{2}} \cdot \text{FWMH}_{AC}. \quad (3.A.5)$$

In the presence of chirp, the interferometric autocorrelation function develops curvature in the wings of the signal (∗ in Figure 3.26). When this feature is present, the FWHM of the autocorrelation and of the original pulse no longer have the simple relation given by Equation 3.A.5. The central peak of the autocorrelation signal will become narrower because the red-shifted, leading portion of the pulse will only incompletely interfere with the blue-shifted tail. The electric field of a linearly chirped pulse can be described as

$$E(t) = E_0\, e^{-\frac{t^2}{a^2} + i2\pi\nu_0 t - ibt^2} \quad (3.A.6)$$

where b is a measure of the chirp. The experimentally obtained autocorrelation must be fit to the autocorrelation that is calculated (Equations 3.A.2 and 3.A.6) with the two parameters, a and b, taken as variables in order to determine the pulse length. In practice, for two-photon microscopy, an absolute measurement of the chirp is generally not necessary. One typically only adjusts the laser to minimize the curvature in the wings of the autocorrelation signal.

ACKNOWLEDGMENTS

REFERENCES

1. Denk, W. and Svoboda, K., Photon upmanship: Why multiphoton imaging is more than a gimmick, *Neuron* 18, 351–357, 1997.

2. Svoboda, K. and Yasuda, R., Principles of two-photon excitation microscopy and its applications to neuroscience, *Neuron* 50, 823–839, 2006.
3. Kleinfeld, D. et al., Fluctuations and stimulus-induced changes in blood flow observed in individual capillaries in layers 2 through 4 of rat neocortex, *Proceedings of the National Academy of Sciences USA* 95, 15741–15746, 1998.
4. Denk, W. et al., Anatomical and functional imaging of neurons and circuits using two photon laser scanning microscopy, *Journal of Neuroscience Methods* 54, 151–162, 1994.
5. Helmchen, F. and Denk, W., Deep tissue two-photon microscopy, *Nature Methods* 2, 932–940, 2005.
6. Denk, W. et al., Two-photon laser scanning fluorescence microscopy, *Science* 248, 73–76, 1990.
7. Denk, W. et al., Two-photon molecular excitation in laser-scanning microscopy, in *Handbook of Biological Confocal Microscopy*, Pawley, J. W., Plenum Press, New York, 1995, pp. 445–458.
8. Williams, R. M. et al., Two-photon molecular excitation provides intrinsic 3-dimensional resolution for laser-based microscopy and microphotochemistry, *FASEB Journal* 8, 804–813, 1994.
9. Zipfel, W. R. et al., Nonlinear magic: Multiphoton microscopy in the biosciences, *Nature Biotechnology* 21, 1369–1377, 2003.
10. Webb, W. W., Two photon excitation in laser scanning microscopy, in *Transactions of the Royal Microscopical Society*, Elder, H. Y. Institute of Physics, Bristol, 1990.
11. Helmchen, F. and Denk, W., New developments in multiphoton microscopy, *Current Opinion in Neurobiology* 12, 593–601, 2002.
12. Yanik, M. F. et al., Functional regeneration after laser axotomy, *Nature* 432, 822, 2004.
13. Nishimura, N. et al., Targeted insult to individual subsurface cortical blood vessels using ultrashort laser pulses: Three models of stroke, *Nature Methods* 3, 99–108, 2006.
14. Tsai, P. S. et al., Ultrashort pulsed laser light: A cool tool for ultraprecise cutting of tissue and cells, *Optics and Photonic News* 14, 24–29, 2004.
15. Loesel, F. H. et al., Laser-induced optical breakdown on hard and soft tissues and its dependence on the pulse duration: Experiment and model, *IEEE Journal of Quantum Electronics* 32, 1717–1722, 1996.
16. Vogel, A. and Venugopalan, V., Mechanisms of pulsed laser ablation of biological tissues, *Chemical Reviews* 103, 577–644, 2003.
17. Joglekar, A. P. et al., Optics at critical intensity: Applications to nanomorphing, *Proceedings of the National Academy of Sciences USA* 101, 5856–5861, 2004.
18. Tsai, P. S. et al., Principles, design, and construction of a two photon laser scanning microscope for *in vitro* and *in vivo* brain imaging, in *In Vivo Optical Imaging of Brain Function*, Frostig, R. D. CRC Press, Boca Raton, 2002, pp. 113–171.
19. Kim, K. H. et al., High-speed, two-photon scanning microscope, *Applied Optics* 38, 6004–6009, 1999.
20. Duemani-Reddy, G. et al., Three-dimensional random access multiphoton microscopy for functional imaging of neuronal activity, *Nature Neuroscience* 11, 713–720, 2008.
21. Vucinić, D. and Sejnowski, T. J., A compact multiphoton 3D imaging system for recording fast neuronal activity, *PLoS ONE* 2, e699, 2007.
22. Denk, W., Two-photon scanning photochemical microscopy: Mapping ligand-gated ion channel distributions, *Proceedings of the National Academy of Sciences USA* 91, 6629–6633, 1994.
23. Potter, S. M., Two-photon microscopy for 4D imaging of living neurons, in *Imaging Neurons: A Laboratory Manual*, Yuste, R., Lanni, F., and Konnerth, A. Cold Spring Harbor Laboratory Press, Cold Spring Harbor, 2000.
24. Majewska, A. et al., A custom-made two-photon microscope and deconvolution system, *Pflugers Archives* 441, 398–408, 2000.

25. Fan, G. Y. et al., Video-rate scanning two-photon excitation fluorescence microscopy and ratio imaging with cameleons, *Biophysical Journal* 76, 2412–2420, 1999.
26. Nikolenko, V. et al., A two-photon and second-harmonic microscope, *Methods* 30, 3–15, 2003.
27. Lanni, F. and Keller, H. E., Microscopy and microscopic optical systems, in *Imaging Neurons: A Laboratory Manual*, Yuste, R., Lanni, F., and Konnerth, A. Cold Spring Harbor Laboratory Press, Cold Spring Harbor, 2000.
28. Hiraoka, Y. et al., Determination of three-dimensional imaging properties of a light microscope system: Partial confocal behavior in epifluorescence microscopy, *Biophysical Journal* 57, 325–333, 1990.
29. Agard, D. A. et al., Fluorescence microscopy in three dimensions, *Methods in Cell Biology*, 353–377, 1989.
30. Holmes, T. J. et al., Light microscopic images reconstructed by maximum likelihood deconvolution, in *Handbook of Confocal Microscopy*, 2nd edition, Pawley, J. B. Plenum Press, New York, pp. 389–402.
31. Kam, Z. et al., Computational adaptive optics for live three-dimensional biological imaging, *Proceedings of the National Academy of Sciences USA* 98, 3790–3795, 2001.
32. Neil, M. A. A. et al., Method of obtaining optical sectioning by using structured light in a conventional microscope, *Optics Letters* 22, 1905–1907, 1997.
33. Lanni, F. and Wilson, T., Grating image systems for optical sectioning fluorescence microscopy of cells, tissues, and small organisms, in *Imaging Neurons: A Laboratory Manual*, Yuste, R., Lanni, F., and Konnerth, A., Cold Spring Harbor Laboratory Press, Cold Spring Harbor, 2000, pp. 8.1–8.9.
34. Bailey, B. et al., Enhancement of axial resolution in fluorescence microscopy by standing-wave excitation, *Nature* 366, 44–48, 1993.
35. Gustafsson, et al., I5M: 3D widefield light microscopy with better than 100 nm axial resolution, *Microscopy* 195, 10–16, 1999.
36. Konig, K. et al., Pulse-length dependence of cellular response to intense near-infrared laser pulses in multiphoton microscopes, *Optics Letters* 24, 113–115, 1999.
37. Centonze, V. E. and White, J. G., Multiphoton excitation provides optical sections from deeper within scattering specimens than confocal imaging, *Biophysical Journal* 75, 2015–2024, 1998.
38. Yariv, A., *Optical Electronics: Third Edition*, Holt, Rinehart and Wilson, New York, 1985.
39. Born, M. and Wolf, E., *Principles of Optics: Electromagnetic Theory of Propagation Interference and Diffraction of Light,* 6th edition, Pergamon Press, Oxford, 1980.
40. Tsai, P. S. et al., All-optical histology using ultrashort laser pulses, *Neuron* 39, 27–41, 2003.
41. Kleinfeld, D. and Denk, W., Two-photon imaging of neocortical microcirculation, in *Imaging Neurons: A Laboratory Manual*, Yuste, R., Lanni, F., and Konnerth, A. Cold Spring Harbor Laboratory Press, Cold Spring Harbor, 2000, pp. 23.1–23.15.
42. Oheim, M. et al., Two-photon microscopy in brain tissue: Parameters influencing the imaging depth, *Journal of Neuroscience Methods* 111, 29–37, 2001.
43. Theer, P. and Denk, W., On the fundamental imaging-depth limit in two-photon microscopy, *Journal of the American Optical Society A* 23, 3139–3150, 2006.
44. Schonle, A. and Hell, S. W., Heating by absorption in the focus of an objective lens, *Optics Letters* 23, 325–327, 1998.
45. Aquirrell, J. M. et al., Long-term two-photon fluorescence imaging of mammalian embryos without compromising viability, *Nature Biotechnology* 17, 763–767, 1999.
46. Koester, H. J. et al., Ca^{2+} fluorescence imaging with pico- and femtosecond two-photon excitation: Signal and photodamage, *Biophysical Journal* 77, 2226–2236, 1999.
47. Patterson, G. H. and Piston, D. W., Photobleaching in two-photon excitation microscopy, *Biophysical Journal* 78, 2159–2162, 2000.

48. Neher, E. and Hopt, A., Highly nonlinear photodamage in the two-photon fluorescence microscopy, *Biophysical Journal* 80, 2029–2036, 2001.
49. Siegman, A. E., *Lasers*, University Science Books, Sausalito, 1986.
50. Fork, R. L. et al., Negative dispersion using pairs of prisms, *Optics Letters* 9, 150–152, 1984.
51. Squier, J. A. et al., Effect of pulse phase and shape on the efficiency of multiphoton processes: Implications for fluorescence microscopy, in *Conference on Lasers and Electro-Optics,* Optical Society of America, Baltimore, 1999, pp. 80.
52. Cerullo, G. et al., High-power femtosecond chirped pulse excitation of molecules in solution, *Chemical Physics Letters* 262, 362–368, 1996.
53. Kawano, H. et al., Attenuation of photobleaching in two-photon excitation fluorescence from green fluorescent protein with shaped excitation pulses, *Biochemical and Biophysical Research Communications* 311, 592–596, 2003.
54. Trebino, R. et al., Measuring ultrashort laser pulses in the time-frequency domain using frequency-resolved optical gating, *Review of Scientific Instrumentation* 68, 3277–3295, 1997.
55. Mainen, Z. F. et al., Two-photon imaging in living brain slices, *Methods* 18, 231–239, 1999.
56. Xu, C. et al., Multiphoton fluorescence excitation: New spectral windows for biological nonlinear microscopy, *Proceedings of the National Academy of Sciences USA* 93, 10763–10768, 1996.
57. Stosiek, C. et al., *In vivo* two-photon calcium imaging of neuronal networks, *Proceedings of the National Academy of Sciences USA* 100, 7319–7324, 2003.
58. Fink, C. et al., Intracellular fluorescent probe concentrations by confocal microscopy, *Biophysical Journal* 75, 1648–1658, 1998.
59. Backus, S. et al., 0.2-TW laser system at 1 kHz, *Optics Letters* 22(16), 1256–8, 1997.
60. Shockley, W. and Pierce, J. R., A theory of noise for electron multipliers, *Proceedings of the Institute of Radio Engineers* 26, 321–332, 1938.
61. Pologruto, T. A. et al., ScanImage: Flexible software for operating laser scanning microscopes, *Biomedical Engineering Online* 17, 13, 2003.
62. Nguyen, Q.-T. et al., MPScope: A versatile software suite for multiphoton microscopy, *Journal of Neuroscience Methods* 156, 351–359, 2006.
63. Gobel, W. and Helmchen, F., New angles on neuronal dendrites in vivo, *Journal of Neurophysiology* 98, 3770–3779, 2007.
64. Göbel, W. et al., Imaging cellular network dynamics in three dimensions using fast 3D laser scanning, *Nature Methods* 4, 73–79, 2007.
65. Loesel, F. H. et al., Non-thermal ablation of neural tissue with femtosecond laser pulses, *Applied Physics B* 66, 121–128, 1998.
66. Stuart, B. C. et al., Nanosecond-to-femtosecond laser-induced breakdown in dielectrics, *Physical Review B* 53, 1749–1761, 1996.
67. Muller, M. et al., Measurement of femtosecond pulses in the focal point of a high-numerical-aperture lens by two-photon absorption, *Optics Letters* 20, 1038–1040, 1995.
68. Diels, J.-C. M. et al., Control and measurement of ultrashort pulse shapes (in amplitude and phase) with femtosecond accuracy, *Applied Optics* 24, 1270–1282, 1985.
69. Kleinfeld, D. et al., Targeted occlusion to surface and deep vessels in neocortex via linear and nonlinear optical absorption, in *Animal Models of Acute Neurological Injuries*, Chen, J., Xu, Z., Xu , X.-M., and Zhang, J. The Humana Press, Inc., Totowa, 2008.
70. Oliva, A. A. Jr. et al., Novel hippocampal interneuronal subtypes identified using transgenic mice that express green fluorescent protein in GABAergic interneurons, *Journal of Neuroscience* 20, 3354–3368, 2000.
71. Zeng, F. et al., Sub-cellular precision on-chip small-animal immobilization, multi-photon imaging and femtosecond-laser manipulation, *Lab on a Chip* 8, 653–656, 2008.
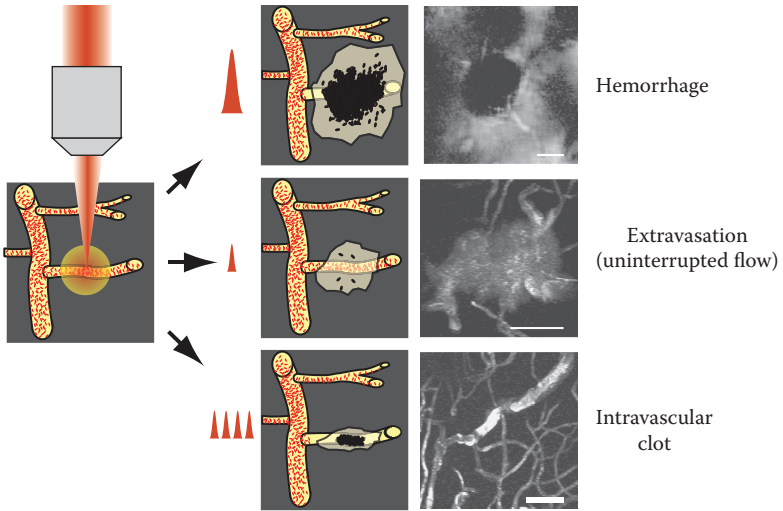
(a) Targeted subsurface microvascular disruption
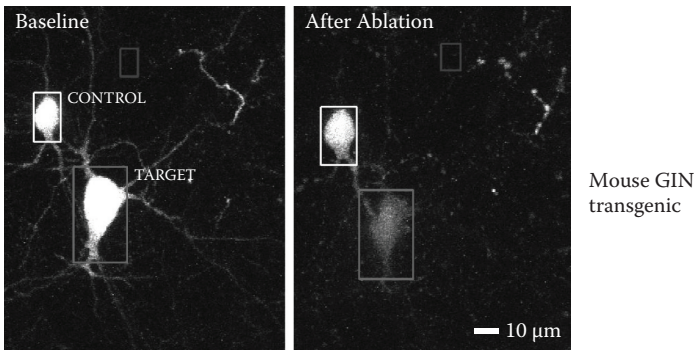
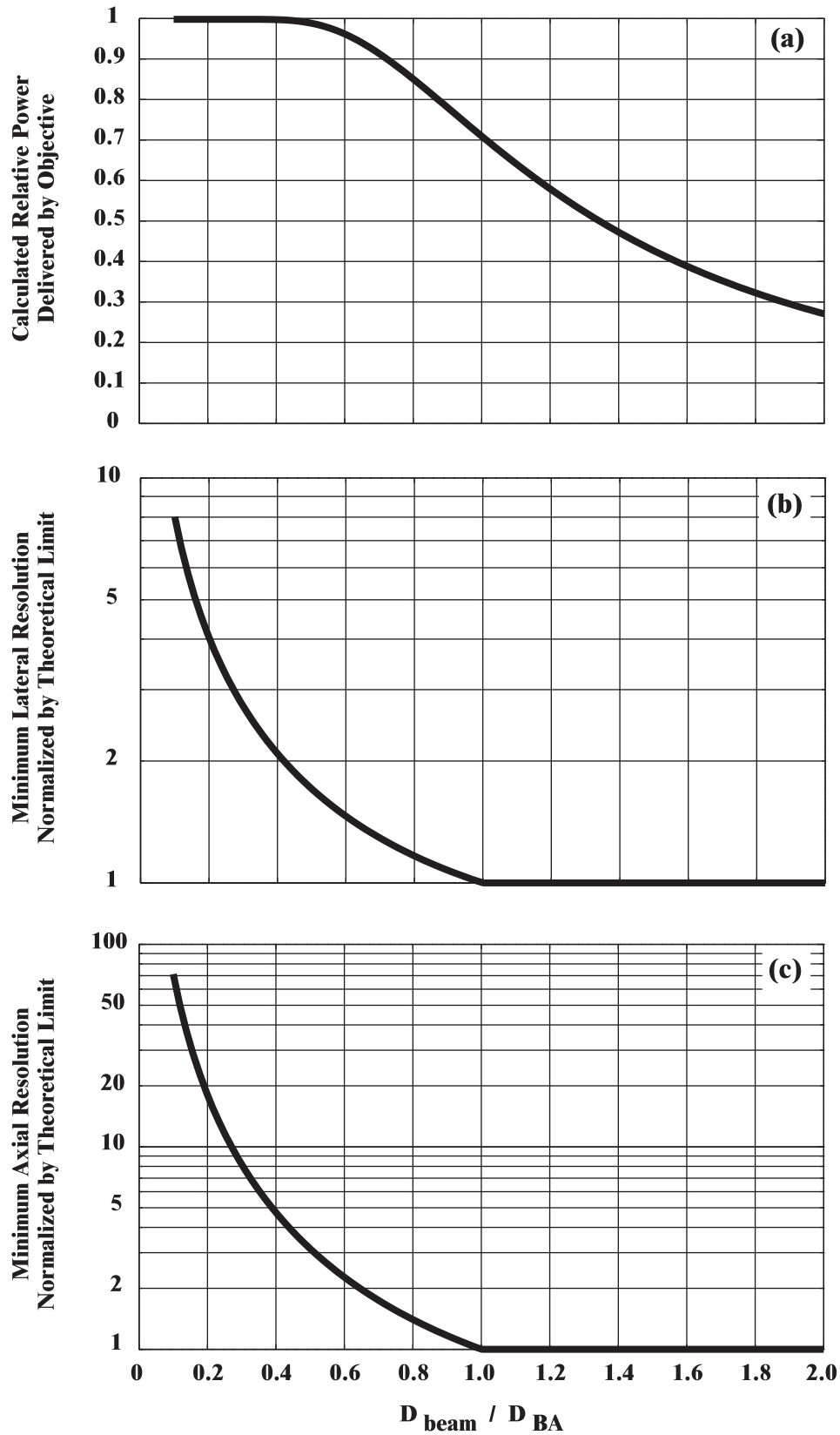(b) Targeted somatic ablation

FIGURE 3.30

Figure 7 Revised - Tsai and Kleinfeld - CRC 2009

Final corrections to Chapter 3; Tsai and Kleinfeld, 28 February 2009

pg 63, Table 3.1, Column 4
from $*\lambda$
to $\sim\lambda$

pg 67, line 5
from $F^{incident}(r,z) \equiv$ Incident laser pulse
to $F^{incident}(r,z) \equiv$ Incident laser pulse fluence

page 69, lines 4-5
from   .... over which the incident light remains essentially undeflected.
to   … over which an e-fold of the incident light is scattered away.

pg 71, figure 3.3, Ed: Replace entire caption with the new caption below.
Pulses with different characteristics can have the same full-width half-maximal spectral width, indicated by $\Delta\lambda$. For illustrative purposes, the pulse widths are 10-times shorter than for those typically used in TPLSM experiments. (a) A pulse with an exponential spectral envelope and the corresponding Lorentzian temporal pulse shape with a full-width half-maximal pulse width of t_P^{FWHM}. (b) A pulse with a Gaussian spectral envelope and the corresponding Gaussian pulse shape. (c) A pulse in which the constituent frequency components are non-uniformly distributed, i.e., chirped. The extent of the chirp has been grossly exaggerated from typical conditions.

pg 73, line 2
from   … .factor of e^{-1}.
to   … factor of e^{-2}.

pg 73, Figure 3.5 caption, line 2
from   A Galleon telescope ...
to   A Galilean telescope ...

pg 76, figure 3.7, replace the figure with the one supplied.

pg 78, figure 3.9 caption, line 3
from   ... depicts the …
to   ... depict the …

pg 79, line 11
from   … the separation, d_2, for six different ...
to   … the separation, d_3, for six different ...

pg 80, line 38
from   ... telescope optics between ...
to   ... telescope between ...

pg 86, line 4
from   ... for width ...
to   … for the pulse width ...

pg 86, line 13
from   ... Green 1[57], from ...
to   ... Green 1,[57] from ...

pg 86, line 14
from   … Fura-2[58,] and up …
to   … Fura-2,[58] and up …

pg 86, line 18
from   … is $\beta^2 = 0.6^7$. The cross-section …
to   … is $\beta^2 = 0.6.^7$ The cross-section …

pg 98, line 9
from   ... which is far best for ...
to   ... which is best for ...

pg 98, line 14
from   ... current in a scanning system is ...
to   ... current generated from a typical raster scan pattern is ...

pg 93, line 1
from   ... 25-mm^2 beamsplitter that ...
to   ... 25-mm beamsplitter cube that ...

pg 106, line 13
from   A unique ...
to   An unique ...

pg 107, Figure 3.29 caption, line 3
from   A) An single ...
to   A) A single ...

pg 107, line 10
from   ... using 40-times ...
to   ... using a 40-times ...

pg 108, Figure 3.30 caption, line 1
clarify or remove "(See color insert following XXX)"

pg 109, lines 25-26
from   ... Technology (Rochester, NY), additional ...
to   ... Technology, additional ...

pg 111, line 10
from   ... (* in Figure 3.26) ...
to   ... (* in Figure 3.27) ...

pg 111, line 26
from   ... spectrum in Figure 3.27, ...
to   ... spectrum in Figure 3.28, ...